The Astrophysical Journal, 988:183 (22pp), 2025 August 1
https://doi.org/10.3847/1538-4357/ade22f

Fundamental Parameters for Central Stars of 103 Infrared Bow Shock Nebulae

Nikhil Patten[1], Henry A. Kobulnicky[1], Matthew S. Povich[2], Angelica S. Whisnant[2,3], Sydney Andrews[1,4],
Alexandra Boone[1], Srujan Dandu[1], Naomi Jones[1], S. Nick Justice[1], Dylan Hope[1,2], Alexander Larsen[1],
Ryan McCrory[1,5], Julia Meredith[1,6], Maria Renee Meza[7], Alexandra C. Rosenthal[1,7,8], William Salazar[1,2],
Alexander R. Sterling[1,9], Noshin Yesmin[7], and Daniel A. Dale[1]
[1] Department of Physics and Astronomy, University of Wyoming, 1000 E. University Avenue, Laramie, WY 82071, USA
[2] Department of Physics and Astronomy, California State Polytechnic University, 3801 West Temple Ave., Pomona, CA 91768, USA
[3] Department of Astronomy, Ohio State University, 4055 McPherson Laboratory, 140 West 18th Avenue, Columbus, OH 43210, USA
[4] Department of Physics and Astronomy, Appalachian State University, 525 Rivers Street, Boone, NC 28608, USA
[5] Department of Physics, Rhodes College, 2000 North Pkwy., Memphis, TN 38112, USA
[6] Department of Physics, Juniata College, 1700 Moore Street, Huntingdon, PA 16652, USA
[7] Department of Astronomy, University of Virginia, 530 McCormick Road, Charlottesville, VA 22904, USA
[8] Department of Astronomy and Cornell Center for Astrophysics and Planetary Science, Cornell Univsersity, Ithaca, NY 14853, USA
[9] Department of Physics and Astronomy, University of Notre Dame, 225 Nieuwland Science Hall, Notre Dame, IN 46556, USA

Received 2025 May 2; revised 2025 June 3; accepted 2025 June 4; published 2025 July 23

Abstract

Stellar bow shock nebulae are arcuate shock fronts formed by the interaction of radiation-driven stellar winds and the relative motion of the ambient interstellar material. Stellar bow shock nebulae provide a promising means to measure wind-driven mass loss, independent of other established methods. In this work, we characterize the stellar sources at the center of bow shock nebulae drawn from all-sky catalogs of 24 μm–selected nebulae. We obtain new, low-resolution blue optical spectra for 104 stars and measure stellar parameters temperature $T_{\rm eff}$, surface gravity $\log g$, and projected rotational broadening $v \sin i$. We perform additional photometric analysis to measure stellar radius R_*, luminosity L_*, and visual-band extinction A_V. All but one of our targets are O and early B stars, with temperatures ranging from $T = 16.5$ to 46.8 kK, gravities from $\log g$=2.57 to 4.60, and $v \sin i$ from $<$100 to 400 km s^{-1}. With the exception of rapid rotator ζ Oph, bow shock stars do not rotate at or near critical velocities. At least 60 of 103 (60%) OB bow shock stars are binaries, consistent with the multiplicity fraction of other OB samples. The sample shows a runaway fraction of 23%, with 19 stars having $v_{\rm 2D} \geqslant 25$ km s^{-1}. Of the 19 runaways, at least 15 ($\geqslant$79%) are binaries, favoring dynamical ejection over the binary supernova channel for producing runaways. We provide a comprehensive census of stellar parameters for bow shock stars, useful as a foundation for determining the mass-loss rates for OB-type stars—one of the single most critical factors in stellar evolution governing the production of neutron stars and black holes.

Unified Astronomy Thesaurus concepts: Stellar winds (1636); Stellar mass loss (1613); Massive stars (732); H II regions (694)

Materials only available in the online version of record: figure set, machine-readable tables

1. Introduction

OB stars inject ionizing radiation and mechanical energy into their host galaxies—a process known as stellar feedback. Radiation-driven stellar winds, unique to O- and B-type stars, blow out and shape their local environments. Stellar feedback during the main-sequence and post-main-sequence stages of evolution can suppress new star formation within a few parsecs from massive stars (M. R. Krumholz & J. C. Tan 2007; G. M. Olivier et al. 2021). In large groups, their combined effects on their host galaxy can even give rise to galactic-scale outflows, known as galactic fountains or chimneys (T. M. Heckman et al. 1993; M. Dahlem et al. 1997). At the end of the main sequence, following significant post-main-sequence evolution, many OB stars undergo core-collapse supernovae. This process, too, can inhibit star formation as the blast waves heat and disrupt nearby molecular clouds (B. Körtgen et al. 2016). After their final act, OB stars leave black holes and neutron stars. This is of particular interest in the era of time-domain astronomy with the advent of gravitational-wave detectors (LIGO, B. P. Abbott et al. 2009; VIRGO, C. Bradaschia et al. 1990) and proposed future missions (LISA; K. G. Arun et al. 2022), which allows the study of these degenerate objects and their mergers. Understanding all of these phenomena requires an understanding of the processes that govern the evolution of massive stars.

The rate at which stars lose mass by radiation-driven stellar winds is a significant factor that determines their evolution. For single-star systems, wind-driven mass loss is the primary determining factor that dictates the star's evolutionary trajectory at the end of the main sequence. The magnitude of mass loss varies during the main-sequence and post-main-sequence stages of evolution. Several techniques for measuring mass-loss rates have been developed, including H profile analysis (R. I. Klein & J. I. Castor 1978; C. Leitherer 1988; H. J. G. L. M. Lamers & C. Leitherer 1993), UV spectroscopy of metal-resonance lines (C. D. Garmany et al. 1981; I. D. Howarth & R. K. Prinja 1989; A. W. Fullerton et al. 2006; W. L. F. Marcolino et al. 2009), and thermal radio/far-IR continuum analyses (D. C. Abbott et al. 1980; P. Benaglia et al. 2007; D. Massa et al. 2017). Measured mass-loss rates

$\log \dot{M}$ ($M_\odot$ yr^{-1}) can range from −4 for the most luminous O-type stars to −8 at the limit of detectability for early B dwarfs (J. Puls et al. 1996; M. M. Rubio-Díez et al. 2022). Each of these techniques is subject to its own inherent limitations and uncertainties. One common source of uncertainty is the amount of clumping in the winds. Small-scale density inhomogeneities may lead to overestimates of mass-loss rates by factors of tens or hundreds if not properly taken into account (A. W. Fullerton et al. 2006). Theoretical prescriptions parameterize mass loss as a function of several key stellar parameters: luminosity L_*, terminal wind speed v , stellar mass M_*, effective temperature $T_{\rm eff}$, and metallicity Z_* (J. S. Vink et al. 2001). Competing sets of models can reduce mass-loss predictions by factors of 2–3 (R. Björklund et al. 2021, 2023; J. Krtička et al. 2021).

A new and independent method of measuring mass-loss rates uses OB stars that produce IR bow shock nebulae (H. A. Kobulnicky et al. 2010, 2018, 2019). Stellar bow shock nebulae are arc-shaped circumstellar features most prominent at mid-infrared wavelengths, sometimes also displaying emission in the optical and radio bandpasses. Stellar bow shock nebulae were first discovered by T. R. Gull & S. Sofia (1979) with the detection of arc-shaped H nebulae around two early-type stars. D. van Buren & R. McCray (1988) conducted the first large-scale search for extended arc- and ring-shaped features as seen at 60 and 100 μm using Infrared Astronomical Satellite (IRAS) survey data. These 33 newly discovered features, of which 15 resembled stellar bow shocks, were associated with hot and luminous stars. They proposed that the shock front, visible at 60 μm, is formed as a result of the collision of stellar wind from a star moving supersonically with respect to the ambient interstellar material.[10] The discovery of stellar bow shock nebulae triggered a search for more of these objects in infrared wavelengths. A. Noriega-Crespo et al. (1997b), examining 58 bow shock candidates selected from IRAS survey data, were able to positively identify 20 stellar bow shocks. With the advent of Spitzer Space Telescope (SST), M. S. Povich et al. (2008) reported the discovery of six stellar bow shock nebulae around Galactic star-forming region M17 with GLIMPSE survey data. V. V. Gvaramadze & D. J. Bomans (2008) and V. V. Gvaramadze et al. (2011a) discovered three and seven bow shock nebulae, respectively, by scanning 22.0 μm Wide-field Infrared Survey Explorer (WISE) data around stars ejected from nearby associations. H. A. Kobulnicky et al. (2010) unveiled 10 additional bow shock candidates in their search of SST Cygnus X Legacy Survey data at 8 and 24 μm bands. C. S. Peri et al. (2015) cataloged 45 bow shock nebulae revealed by WISE data. The sample of bow shock nebulae grew to 709 in the extensive search of SST and WISE data in H. A. Kobulnicky et al. (2016). This catalog of bow shock nebulae was expanded with the addition of 310 new candidates from a citizen-science search of SST archival data (T. Jayasinghe et al. 2019). H. A. Kobulnicky et al. (2019), following the procedure of H. A. Kobulnicky et al. (2010, 2018), demonstrated the promise of using the physics and geometry of bow shock nebulae to measure mass-loss rates in their study of 70 stars at the center of bow shock nebulae (shortened to bow shock stars for the remainder of this work).

W. T. Chick et al. (2020) conducted a spectroscopic study on a subsample of 84 bow shock stars from the H. A. Kobulnicky et al. (2016) catalog. Red−optical spectra indicated that 96% (81 of 84) of the studied bow shock stars were early-type stars, confirming the identification of bow shock nebulae as a reliable method of finding previously unknown OB stars. Their spectra allowed them to obtain rough spectral classification, with stars categorized as O, OB, or B type. However, their data precluded reliable luminosity classification. At least $\gtrsim$36% of the sampled stars also showed radial velocity variations, indicating that a significant fraction of bow shock stars were in multiple systems. H. A. Kobulnicky & W. T. Chick (2022) studied the kinematics for 267 bow shock stars using Gaia EDR3 proper-motion data (Gaia Collaboration 2020). Surprisingly, only 24% were determined to be runaways, while the remaining 76% of stars had 2D space velocities less than 25 km s^{-1}. This result indicated that runaway stars were not the primary driving mechanism in forming bow shock nebulae. Rather, the velocity differential generated from a bulk flow of material or interstellar density enhancements played larger-than-expected roles in the formation of stellar bow shock nebulae.

In this work, we build on the W. T. Chick et al. (2020) study and present the results of a new spectroscopic analysis on a subsample of 104 bow shock stars. This work is the first comprehensive spectroscopic survey of this size for bow shock stars using blue wavelength optical spectra that enables an improved measurement of stellar parameters $T_{\rm eff}$, $\log g$, and $v \sin i$. In Section 2, we discuss target selection from previous bow shock catalogs. In Section 3, we present our methods of extracting stellar parameters from blue−violet optical spectra using grids of theoretical stellar spectra. In Section 4, we present the results of our analysis for the 104 selected bow shock stars. In Section 5, we discuss how bow shock stars compare to non-bow-shock-forming OB stars. In Section 6, we summarize our findings, discuss some of the implications of our work, and offer directions for future bow shock studies.

2. Spectroscopic Observations

2.1. Target Selection

We developed and applied several cuts to the H. A. Kobulnicky et al. (2016) and T. Jayasinghe et al. (2019) catalogs when creating our subsample of bow shock stars to observe. Starting with the 709 bow shock candidates in H. A. Kobulnicky et al. (2016) and 187 of the 310 reported in T. Jayasinghe et al. (2019) (896 in total), we selected stars north of −45° decl. (observable from northern-based observatories), resulting in 589 potential targets. We further selected only targets with parallax-to-parallactic-uncertainty ratios greater than 5 (i.e., reliable distances), resulting in a subsample of 204. The last cut of Gaia G magnitude brighter than 13.5[11] (bright enough to perform sensitive blue−violet spectroscopy) results in a final count of 145 potential target stars. Of these, we obtained spectra for 104 candidates. Table 1 summarizes the parent sample and the subsequent culling of the potential targets.

---

[10] For completeness, other stellar sources can produce bow shock nebulae such as pulsars (P. Hartigan et al. 1987; D. J. Helfand et al. 2001; Z. Wang et al. 2013), X-ray binaries (V. V. Gvaramadze et al. 2011b), low-mass evolved stars (A. Noriega-Crespo et al. 1997a; V. V. Gvaramadze et al. 2014a, 2014b), and Herbig-Haro objects (K. R. Stapelfeldt et al. 1991; C.-F. Lee et al. 2000; J. Bally et al. 2002). These fascinating phenomena are not the subject of this paper.

[11] This corresponds to $B_P = 14$–15 mag, given typical $B_P - G$ colors of 1–2 mag.

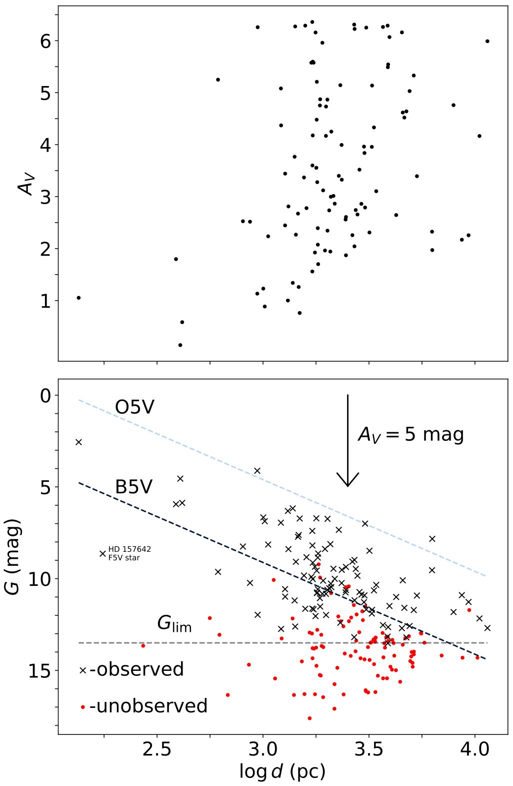

Figure 1. Completeness of bow shock sample.

Figure 1 plots the measured visual extinction A_V (described in Section 3.2) against Gaia DR3 parallactic distance d (top panel) and apparent Gaia G-band magnitude against distance (bottom panel) for the subsample of bow shock stars described above. In the top panel, extinction scales with distance, with scatter due to nonuniform Galactic dust structure. In the bottom panel, black crosses indicate the 104 observed program stars and red circles signify unobserved bow shock candidate stars. Diagonal dashed lines indicate the unreddened apparent magnitudes of an O5 dwarf and a B5 dwarf, respectively (M. J. Pecaut & E. E. Mamajek 2013). The horizontal line illustrates the effective brightness limit of our sample of approximately $G = 13.5$ mag. The vertical arrow designates a typical V-band extinction of 5 mag (converted to Gaia G-band extinction). Targets span distances ranging from 134 pc to 11.5 kpc, with 11 bow shock stars within 1 kpc of the Sun.

Many targets beyond 1 kpc fall below the dim B5 V track. This is expected, as distant stars lie behind large column densities of dust and can exhibit several magnitudes of extinction. It is also important to remind the reader that stars cataloged in H. A. Kobulnicky et al. (2016) and T. Jayasinghe et al. (2019) are *candidate* central stars to the bow shock nebula. In some cases, the identification of the central star is ambiguous from 4.5 μm data. For example, in their spectroscopic study of bow shock stars W. T. Chick et al. (2020) note four cases in which multiple stars reside near the geometric center of the nebula and propose alternative powering stars based on optical spectra and angular distances. For discussion of notable outlier HD 157642, see Appendix B.

Table 1
Starting Samples and Cuts

Catalog and Cuts	Number
K16	709
J19	187 of 310
Total	896
North of -45°	589
Previous + $\pi/\sigma_\pi > 5$	204
Previous + $G < 13.5$	145

Table 2 presents an overview of the 104 bow shock stars observed. Column (1) is the identification number of the bow shock nebula from the 709 objects cataloged in H. A. Kobulnicky et al. (2016) and an additional 310 nebulae from T. Jayasinghe et al. (2019). Column (2) is a common alias of the star, where available. Columns (3) and (4) are the R.A. and decl. of the program stars in J2000 coordinates. Column (5) is the Gaia B_P magnitude of the star. Column (6) indicates the observatory used. Most of the stars were observed at Apache Point Observatory (APO), but six stars were observed from Wyoming Infrared Observatory (WIRO). Column (7) provides the number and duration of exposures.

The target stars reside almost entirely within 1° of the Galactic plane (see Figure 3 of H. A. Kobulnicky et al. 2016), with the notable exception of the nearby bow shock star ζ Oph lying 24° above the plane. Figure 2 plots the Galactic longitude of the 104 target stars in a polar representation with the Sun at the center and Galactic center toward the right. The radial distance from the center indicates heliocentric distance, derived from Gaia EDR3 inverse parallaxes. Distances range from 134 pc to 11.5 kpc, with a median distance of 2 kpc. For viewing purposes, the plot in Figure 2 is limited to only show targets within 9 kpc.

We performed observations of 28 well-studied, nonprogram OB stars. These stars, referred to hereafter as the comparison sample, were observed to compare the retrieved stellar parameters in this work with those in other published works. We selected them on the basis of being OB-type stars with previously measured values for stellar parameters ($T_{\rm eff}$, $\log g$, and $v \sin i$), as well as having bright apparent magnitudes ($B_P < 10$ mag). As a result of these selection criteria, the comparison sample largely overlaps with stars cataloged in the `IACOB` project (S. Simón-Díaz et al. 2011).

2.2. Spectrograph Configuration

Observations were carried out at APO with the 3.5 m telescope and at WIRO with the 2.3 m telescope. Observations at APO were performed with the KOSMOS spectrograph. At APO, we used the blue 704 line mm^{-1} second-order grism, yielding a reciprocal dispersion of 0.68 Å pixel^{-1}. The $0\farcs83 \times 360$ slit produced spectra with resolution $R = 2200$ and spectral coverage 3700–6200 Å.[12] The long-slit spectrograph at WIRO used a 600 line mm^{-1} grating in second order with the $1\farcs2 \times 120$ slit. This configuration yielded a reciprocal dispersion of 1.10 Å pixel^{-1}, resolution $R = 1500$, and coverage of 4000–5800 Å.

We performed wavelength calibrations with the internal Kr and Ar calibration lamps at APO, yielding solutions with an rms of 0.06 Å, and with the internal CuAr calibration lamp at WIRO, providing solutions with an rms of 0.05 Å. We obtained multiple comparison-lamp exposures throughout the

---

[12] On a few nights, the $0\farcs87$ slit was used, yielding similar resolution and wavelength coverage.

Table 2
Observations

SBN ID (1)	Alias (2)	R.A. (2000) (HH:MM:SS) (3)	Decl. (2000) (°: :) (4)	B_P (mag) (5)	Observatory (6)	Exposures (7)
001$_\star$	CD −29 14004	17:48:07.68	−29:07:55.6	11.24	APO	3 × 300 s
007$_\star$	⋯	17:58:30.65	−26:09:49.3	13.39	APO	1 × 600 s
010$_\star$	HD 314937	18:00:17.47	−25:14:14.6	10.95	APO	2 × 300 s
013$_\star$	ζ Oph	16:37:09.55	−10:34:01.2	3.01	APO	1 × 10 s
016$_\star$	⋯	18:00:55.22	−22:57:37.1	12.76	APO	1 × 900 s
019$_\star$	⋯	18:05:11.18	−21:04:43.3	13.14	APO	1 × 1200 s
026$_\star$	⋯	18:11:59.40	−19:36:55.4	12.63	APO	1 × 150 s
027$_\star$	TYC 6272-1457-1	18:12:13.03	−19:35:24.0	11.24	APO	1 × 150 s
039$_\star$	⋯	18:08:46.42	−16:25:59.5	13.01	APO	1 × 900 s
043$_\star$	TYC 6269-2270-1	18:16:25.25	−17:05:20.8	11.78	APO	1 × 900 s
051$_\star$	NGC 6618 258	18:20:22.70	−16:08:34.1	13.74	APO	2 × 900 s
054$_\star$	HD 165319	18:05:58.82	−14:11:53.2	8.06	WIRO	3 × 90 s
056$_\star$	⋯	18:17:17.18	−15:29:25.4	12.69	APO	1 × 600 s
061$_\star$	HD 168183	18:18:58.70	−13:59:28.3	8.29	APO	2 × 60 s
063$_\star$	BD −13 4934	18:19:05.57	−13:54:50.4	9.50	APO	2 × 180 s
064$_\star$	BD −14 5040	18:25:38.90	−14:45:05.8	10.68	APO	1 × 300 s
065$_\star$	BD −13 4937	18:19:20.04	−13:54:21.6	10.81	APO	1 × 600 s
066$_\star$	⋯	18:15:23.98	−13:19:35.8	12.04	APO	1 × 300 s
067$_\star$	NGC 6611 584	18:18:23.64	−13:36:28.1	12.33	APO	1 × 600 s
150$_\star$	TYC 5118-279-1	18:49:25.06	−02:21:09.7	10.75	APO	1 × 300 s
200$_\star$	⋯	19:02:08.86	3:30:47.2	14.11	APO	2 × 900 s
240$_\star$	HD 230561	19:03:40.70	13:03:11.9	10.96	APO	1 × 300 s
255$_\star$	TYC 1054-952-1	19:19:00.82	13:42:59.0	11.58	APO	2 × 360 s
288$_\star$	HD 350123	19:32:44.33	19:58:40.8	11.26	APO	2 × 360 s
298$_\star$	HD 345117	19:51:08.18	22:49:54.5	9.23	WIRO	2 × 600 s
300$_\star$	HD 344765	19:44:20.06	23:52:45.1	10.91	WIRO	1 × 600 s
302$_\star$	LS II +23 47	19:45:47.52	24:06:00.0	11.12	WIRO	1 × 600 s
303$_\star$	⋯	19:46:06.17	24:11:13.9	14.29	APO	2 × 1800 s
305$_\star$	HD338936	19:46:22.68	24:37:48.0	10.21	WIRO	1 × 600 s
306$_\star$	BD +24 3883	19:47:21.38	24:33:43.9	10.42	WIRO	2 × 600 s
314$_\star$	HD 338961	19:50:24.41	27:27:55.8	11.04	APO	1 × 180 s
319$_\star$	⋯	20:05:38.11	36:39:38.2	12.87	APO	1 × 900 s
320$_\star$	HD 191611	20:09:26.06	36:29:19.7	8.66	APO	2 × 45 s
321$_\star$	⋯	20:14:33.29	36:29:49.9	14.06	APO	4 × 900 s
322$_\star$	⋯	20:14:51.10	36:35:58.2	13.51	APO	3 × 900 s
324$_\star$	LS II +38 19	20:13:28.92	38:14:31.6	11.41	APO	2 × 45 s
325$_\star$	HD 194303	20:23:35.71	36:55:44.0	8.79	APO	1 × 240 s
326$_\star$	TYC 2697-1046-1	20:32:56.26	36:12:00.4	11.37	APO	1 × 300 s
328$_\star$	⋯	20:35:34.44	36:34:25.3	12.55	APO	2 × 45 s
330$_\star$	HD 229159	20:22:54.02	39:12:28.8	8.78	APO	2 × 240 s
331$_\star$	LS II +39 53	20:27:17.57	39:44:32.6	10.55	APO	2 × 300 s
332$_\star$	⋯	20:26:24.89	40:01:41.2	12.76	APO	3 × 480 s
335$_\star$	TYC 3156-1106-1	20:28:15.38	40:44:04.6	11.51	APO	2 × 360 s
339$_\star$	⋯	20:36:04.51	40:56:13.2	13.01	APO	2 × 500 s
340$_\star$	HD 195229	20:28:30.24	42:00:35.3	7.68	APO	2 × 45 s
341$_\star$	⋯	20:34:28.94	41:56:16.8	13.36	APO	5 × 900 s
343$_\star$	⋯	20:30:34.97	44:18:54.7	7.25	APO	1 × 45 s
344$_\star$	BD +43 3654	20:33:36.07	43:59:07.4	7.58	APO	2 × 300 s
345$_\star$	HD 199021	20:52:53.21	42:36:27.7	8.58	APO	1 × 180 s
346$_\star$	⋯	20:51:50.21	43:19:29.6	13.70	APO	3 × 900 s
349$_\star$	LS III +49 20	21:21:39.07	50:02:01.0	11.37	APO	1 × 900 s
350$_\star$	⋯	21:22:55.70	50:24:25.2	13.35	APO	3 × 480 s
351$_\star$	TYC 3979-1998-1	22:12:30.07	55:32:07.4	11.49	APO	2 × 600 s
353$_\star$	⋯	22:16:32.93	59:23:30.8	12.36	APO	2 × 900 s
354$_\star$	⋯	22:27:41.42	57:41:04.6	12.49	APO	2 × 900 s
356$_\star$	HD 240015	22:39:17.71	59:01:00.5	10.18	APO	2 × 300 s
357$_\star$	HD 240016	22:39:22.54	59:00:25.9	9.84	APO	1 × 300 s
358$_\star$	TYC 4264-1036-1	22:34:06.50	60:58:50.2	10.65	APO	2 × 300 s
359$_\star$	HD 215806	22:46:40.22	58:17:43.8	9.30	APO	1 × 300 s
360$_\star$	HD 216411	22:51:33.77	59:00:30.6	7.35	APO	2 × 30 s
361$_\star$	TYC 4278-522-1	22:51:39.72	61:08:51.0	10.89	APO	2 × 600 s
362$_\star$	⋯	22:55:45.4	60:24:40.3	13.69	APO	6 × 900 s

Table 2
(Continued)

SBN ID (1)	Alias (2)	R.A. (2000) (HH:MM:SS) (3)	Decl. (2000) (°: :) (4)	B_P (mag) (5)	Observatory (6)	Exposures (7)
364$_\star$	BD +60 39	00:21:53.88	61:45:02.5	9.49	APO	1 × 600 s
365$_\star$	HD 2619	00:30:28.32	65:16:19.6	8.43	APO	3 × 100 s
366$_\star$	HD 2083	00:25:51.24	71:48:25.6	6.85	APO	2 × 30 s
367$_\star$	TYC 4046-1614-1	02:17:53.21	61:11:12.8	11.16	APO	2 × 360 s
368$_\star$	V* KM Cas	02:29:30.46	61:29:44.2	11.49	APO	2 × 360 s
369$_\star$	BD +60 586	02:54:10.68	60:39:03.6	8.52	APO	1 × 180 s
371$_\star$	TYC 3339-851-1	04:05:53.04	51:06:58.0	11.91	APO	1 × 600 s
372$_\star$	TYC 3340-2437-1	04:11:10.73	50:42:29.5	11.55	APO	1 × 600 s
373$_\star$	HD 21856	03:32:40.01	35:27:42.1	5.82	APO	2 × 60 s
374$_\star$	HD 41161	06:05:52.44	48:14:57.5	6.66	APO	3 × 45 s
375$_\star$	V* AE Aur	05:16:18.14	34:18:45.0	6.08	APO	1 × 30 s
376$_\star$	HD 48099	06:41:59.23	06:20:43.4	6.27	APO	1 × 30 s
377$_\star$	HD 46573	06:34:23.57	02:32:03.1	8.00	APO	1 × 120 s
378$_\star$	υ Ori	05:31:55.85	−07:18:05.8	4.55	APO	1 × 15 s
381$_\star$	HD 54662	07:09:20.26	−10:20:47.8	6.16	APO	1 × 45 s
383$_\star$	CD −26 5136	07:53:01.01	−27:06:57.6	9.75	APO	1 × 360 s
384$_\star$	CD −35 4415	08:16:32.09	−35:38:52.8	10.72	APO	1 × 550 s
385$_\star$	CD −41 4637	08:55:27.67	−41:35:22.2	9.95	APO	1 × 720 s
386$_\star$	V* GP Vel	09:02:06.86	−40:33:16.9	7.00	APO	3 × 45 s
388$_\star$	HD 75860	08:50:53.23	−43:45:05.4	7.79	APO	1 × 180 s
389$_\star$	HD 76031	08:52:04.13	−44:00:34.9	9.11	APO	1 × 600 s
634$_\star$	HD 152756	16:57:15.00	−43:43:15.2	9.19	APO	1 × 300 s
640$_\star$	HD 326533	16:58:24.05	−42:43:41.2	10.23	APO	1 × 300 s
662$_\star$	HD 153426	17:01:13.01	−38:12:11.9	7.46	APO	1 × 120 s
667$_\star$	V* V1012 Sco	17:15:22.32	−38:12:46.8	6.64	APO	1 × 120 s
673$_\star$	…	17:20:38.23	−38:01:48.7	14.71	APO	2 × 1200 s
687$_\star$	…	17:28:59.78	−36:06:54.7	14.41	APO	2 × 1200 s
692$_\star$	…	17:27:11.23	−34:14:35.2	11.73	APO	3 × 300 s
700$_\star$	…	17:33:47.88	−31:16:27.1	14.30	APO	2 × 1200 s
705$_\star$	CD −29 13925	17:45:08.21	−29:56:45.2	10.93	APO	1 × 600 s
2G0063185-0066622$_\star$	…	18:02:29.23	−23:49:34.0	12.78	APO	2 × 500 s
2G0065094-0061344$_\star$	…	18:02:41.88	−23:38:02.0	12.84	APO	2 × 900 s
2G0118310-0062990$_\star$	HD 166965	18:13:51.38	−18:59:22.2	8.78	APO	2 × 120 s
2G0592097+0012519$_\star$	…	19:41:43.08	23:16:01.9	12.87	APO	2 × 400 s
2G0600615-0018340$_\star$	HD 344878	19:44:44.06	23:51:07.9	10.72	APO	2 × 300 s
2G0770694+0193568$_\star$	HD 193427	20:18:45.17	39:24:22.3	9.31	APO	2 × 300 s
2G1045666+0128085$_\star$	BD +57 2513	22:22:02.57	58:43:09.5	9.76	APO	1 × 300 s
…	κ Cas	00:33:00.00	62:55:54.5	4.17	APO	2 × 10 s
2G3525610+0001887$_\star$	CD −35 11561	17:26:36.10	−35:11:32.3	11.97	APO	1 × 600 s
2G3527642+0032660$_\star$	HD 157642	17:25:54.60	−34:51:05.8	8.91	APO	1 × 120 s
2G3533026+0008095$_\star$	HD 319881	17:28:21.67	−34:32:30.5	10.32	APO	1 × 600 s
2G3585210+0089852$_\star$	…	17:38:32.28	−29:43:07.0	12.69	APO	1 × 60 s

Note. Column (1): stellar bow shock nebula identifier from H. A. Kobulnicky et al. (2016) and addendum T. Jayasinghe et al. (2019) catalogs. Column (2): common alias, if available. Column (3): R.A., in HH:MM:SS. Column (4): decl., in DD:MM:SS. Column (5): Gaia B_P magnitude. Column (6): observatory used, either APO or WIRO. Column (7): number of exposures and the length of the exposures.

(This table is available in machine-readable form in the online article.)

night and applied an interpolated wavelength solution to science frames to remove the effect of instrument flexure on the wavelength solutions. We divided science images in `iraf` by flat fields obtained from quartz dome lamp exposures. Spectra were then normalized and combined using tasks in the `specred` package. At APO, exposure times of 2 × 45 s and 2 × 1200 s for $B_P = 8.7$–14.3 mag targets yielded spectra with continuum signal-to-noise ratios (SNRs) of 90:1 and 30:1 pixel^{-1} at 4200 Å, respectively. SNR was heavily dependent on seeing conditions, and two to three spectra were often obtained in the same night and combined in the reduction process to maximize the SNR. We calculated heliocentric offsets and shifted spectra to that frame of reference. Examining a subsample of 13 stars from the comparison sample, we compared our derived radial velocities with those found in other works. Our radial velocities are scattered about the literature values with an rms of 30 km s^{-1}. Due to the low R of the instrument, we do not attempt to measure radial velocities to a high degree of precision.

Figure 3 presents the spectrum of bright bow shock nebula central star ζ Ophiuchi—identifier BS013 in the H. A. Kobulnicky et al. (2016) catalog—with normalized intensity plotted against wavelength. Atomic transitions sensitive to changes in stellar parameters ($T_{\rm eff}$ and $\log g$) in the regime of OB stars are labeled. All program stars exhibit strong Balmer features and He I transitions, as is typical for OB stars. Many bow shock

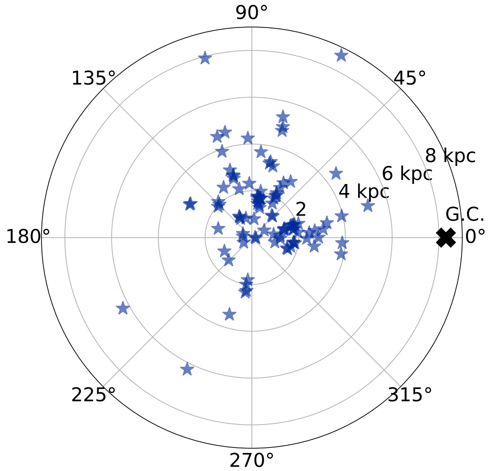

Figure 2. Observed program stars (indicated by blue stars) plotted on the sky.

stars also express absorption in the He II Pickering series, indicating O-type stars. Weaker blended groups of ionized metals, sensitive to changes in luminosity and temperature, are also apparent. Ratios of He II/He I, Si IV/Si III, and Si III/Si II are good indicators of temperature $T_{\rm eff}$, and ratios of Si IV/He I and Si III/He I gauge luminosity L_* (R. O. Gray & J. C. Corbally 2009). Diffuse interstellar absorption bands (DIBs) are present at 4430 and 4727 Å, to varying degrees, in all target spectra. Appendix A contains vertically stacked normalized spectra for all 104 target stars, in order of H. A. Kobulnicky et al. (2016) identifier number for stars drawn from the H. A. Kobulnicky et al. (2016) catalog, and in order of Galactic longitude for stars chosen from the T. Jayasinghe et al. (2019) catalog.

3. Analysis

3.1. Temperature, Gravity, and Rotation from Spectral Fitting

We extracted stellar parameters from spectra with a custom Python grid-search fitting routine. This code compares stellar spectra with a grid of model synthetic spectra from the TLUSTY OSTAR2002 (T. Lanz & I. Hubeny 2003) and BSTAR2006 (T. Lanz & I. Hubeny 2007) libraries, smoothed and interpolated to match the resolution of the data. TLUSTY model spectra spanned $T_{\rm eff}$ from 15 to 30 kK in steps of 1 kK for the BSTAR2006 models and from 27.5 to 55 kK in steps of 2.5 kK for the OSTAR2002 models. Surface gravities $\log g$ ranged from 1.75 to 4.75 in steps of 0.10 for the BSTAR2006 set and from 3.0 to 4.75 in steps of 0.25 for the OSTAR2002 models. We convolved model spectra with instrumental and additional rotational broadenings ranging from 10 to 500 km s^{-1} using the `rotin` IDL code (I. Hubeny & T. Lanz 2011). Our spectral fitting code determines a best-fit model spectrum by comparing the residuals between the input spectrum and all synthetic spectra and selecting the model with the smallest absolute deviation as the best fit. The stellar parameters from the best-fit model spectrum were then used as priors in the next step of the analysis.

After this rudimentary fitting routine, we performed a Bayesian Markov Chain Monte Carlo (MCMC) analysis. MCMC fitting for spectral analysis requires a full characterization of uncertainties. The most eminent contributor to uncertainty in the observed spectrum is the statistical noise of the spectrum, indicated by the SNR at any given pixel. We measured this quantity by following the procedure described in A. Irrgang et al. (2014). We created a histogram of the dispersion, Δ_i, which we define as

$$\Delta_i \equiv f_i - \frac{1}{2}f_{i-2} - \frac{1}{2}f_{i+2}, \tag{1}$$

for all i pixels, with f_i representing the continuum-normalized intensity at the ith pixel. The quantity Δ_i represents the equally weighted deviation between nearby pixels separated by 2 pixels, since adjacent pixels are likely to be correlated. The standard deviation of the Δ_i histogram was used as the empirical statistical uncertainty for the spectrum. Another important source of uncertainty is the systematic uncertainty represented by features in the stellar spectrum that are not present in the model. The source of these systematic differences can be interstellar features (DIBs and Na I doublet at 5890 and 5896 Å, for example), element enhancements from mass transfer and mergers for binary systems (N. Langer 2012; S. E. de Mink et al. 2013), mixing processes (J. G. Rivero González et al. 2012; L. P. Carneiro et al. 2016; N. J. Grin et al. 2017), degree of broadening due to micro- and macroturbulence (M. R. Villamariz & A. Herrero 2000; R. S. I. Ryans et al. 2002; N. Markova & J. Puls 2008), or stellar wind phenomena not included in the TLUSTY models. To obtain an estimation of these systematics, we used the residuals from the best-fit model spectrum and smoothed this residual spectrum by 3 pixels. At each pixel, we computed a complete uncertainty estimation by adding the statistical uncertainty component in quadrature with the systematic uncertainty, as described in I. Czekala et al. (2015). With an empirical estimation of uncertainty at each pixel, the MCMC walkers explored the 3D parameter space of stellar parameters (i.e., $T_{\rm eff}$, $\log g$, and $v \sin i$). At each walker step, our code computes a model spectrum using linear interpolation from the model grid and denotes an associated reduced $\chi^2_{\rm red}$ for this interpolated model, given by the equation

$$\chi^2_{\rm red} = \frac{1}{n_{\rm pix}} \sum_{i=0}^{n_{\rm pix}} \frac{(f_{{\rm data},i} - f_{{\rm model},i})^2}{\sigma_i}, \tag{2}$$

where $f_{{\rm data},i}$ signifies the normalized intensity, $f_{{\rm model},i}$ the normalized intensity of the model spectrum, and σ_i the uncertainty at that pixel, for all i pixels between 4000 and 5000 Å.

Figure 4 plots the posterior distribution of the stellar parameters for the bright O8–9 V star ζ Oph. The shape of the posteriors indicates that the fitted parameters are well constrained with a well-defined preferred solution. The median values for temperature, $\log g$, and $v \sin i$ of 32.1 kK, 3.70, and 375 km s^{-1}, respectively, compare favorably with the reported values of 32.0 kK, 3.71, and 385 km s^{-1} (G. Holgado et al. 2022). The widths of the posterior distributions are measures of uncertainty on each parameter. We chose the 16th- and 84th-percentile values in the explored samples as the 1σ uncertainties. The uncertainties in the fitted stellar parameters (500 K in $T_{\rm eff}$, 0.06 in $\log g$, and 11 km s^{-1} for the test case ζ Oph) represent the range of stellar parameters explored by the MCMC walkers in determining the best-fit stellar model.

Figure 5 shows the results of our fitting process on the spectrum of ζ Oph. The top panel demonstrates the agreement

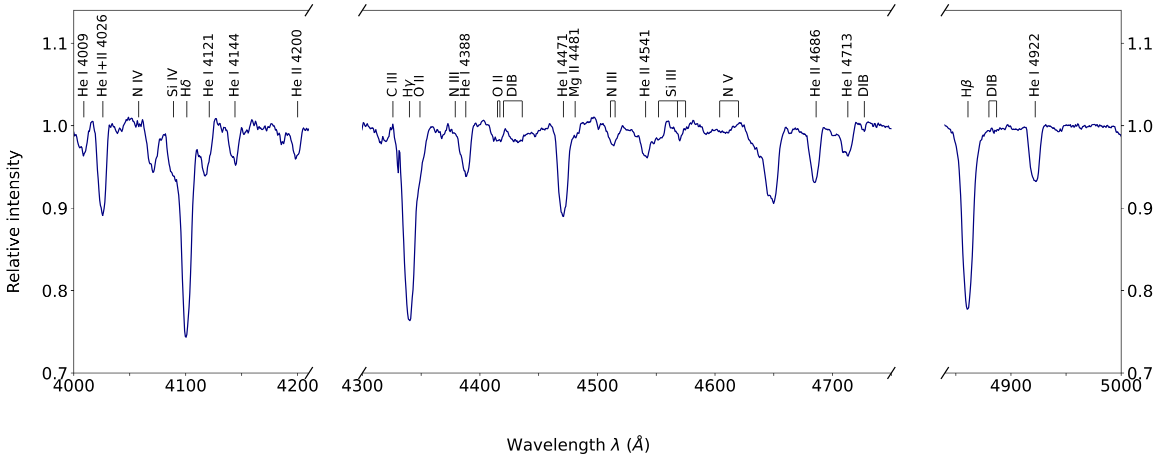

Figure 3. APO spectrum of ζ Oph.

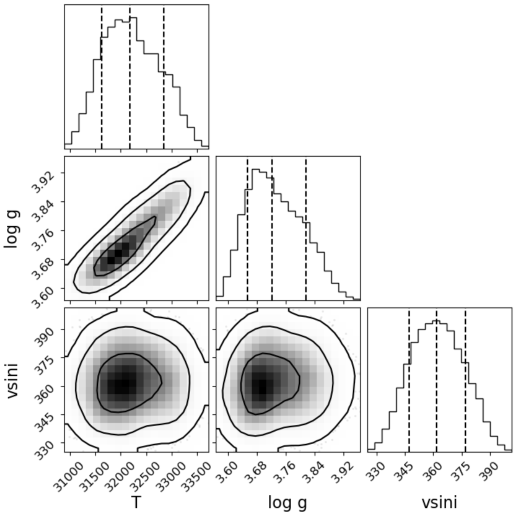

Figure 4. Posterior distribution on stellar parameters.

between the input spectrum (black line) and the best-fit interpolated model (dashed red line). The bottom panel plots the residuals (black line) at each pixel and the 1σ, 2σ, and 3σ uncertainty levels (in decreasing opacities; orange) at each pixel. The 1σ, 2σ, and 3σ uncertainty spectrum displayed in the bottom panel illustrates the uncertainty at each pixel the MCMC code used when evaluating the χ^2_{red} for each sampled model. The residual spectrum is almost completely enveloped by the 1σ uncertainty spectrum, indicating that the uncertainty spectrum is appropriately characterized. The largest deviations between the data and model are within a few percent. Differences in the continuum regions are random and encompassed fully by the statistical noise. Systematic features in the residuals lie at the wavelengths of stellar atmospheric lines that are not well fit by any model. For ζ Oph in particular, these systematic features are predominantly He lines, with the EW observed in the spectrum greater than in the models. An explanation for this mismatch in the case of ζ Oph could be the star's formation history. W. van Rensbergen et al. (1996) propose that ζ Oph is a former secondary member in a previous binary system. Examining proper-motion and evolutionary data, W. van Rensbergen et al. (1996) hypothesized that mass transfer from the primary deposited enriched material onto ζ Oph and spun up the star, creating the He-enriched rapid rotator we observe today. The TLUSTY models are computed with solar $Y_{\text{He}} = 0.10$, as opposed to the measured Y_{He} 0.20 for ζ Oph as found in other works (I. D. Howarth & K. C. Smith 2001; K. Shepard et al. 2022; A. de Burgos et al. 2024). In spite of this, solar abundances are a reasonable assumption given the unknown histories of each of the bow shock stars. Furthermore, metal and helium abundances are not of interest in this study, nor are they readily measurable from low-resolution spectra.

3.2. Mass and Radius from SED Fitting

Stellar spectra provide information on stellar parameters temperature T_{eff}, surface gravity $\log g$, and projected rotational broadening $v \sin i$. Since $\log g$ is dependent on both stellar mass M_* and stellar radius R_*, analysis of the stellar spectra cannot explicitly constrain these parameters. These additional parameters can be obtained by fitting stellar models to broadband, multiwavelength, photometric data, given Gaia EDR3 parallaxes and stellar spectral parameters T_{eff} and $\log g$ as priors. We retrieved photometric data from several astronomical surveys in different wavelength regimes. In the optical, we used Gaia EDR3 G_P, R_P, and B_P and APASS (A. A. Henden et al. 2016) U, B, V, u , g , and r magnitudes. In the near-infrared, we utilized J, H, and K magnitudes from the Two Micron All Sky Survey and W1 and W2 magnitudes from WISE. We used EXOFASTv2 (J. D. Eastman et al. 2019) with the MIST (J. Choi et al. 2016) evolutionary models to obtain fits for stellar radius, evolutionary mass, and visual extinction A_V.

3.3. MK Spectral Typing

In addition to measuring fundamental stellar parameters temperature T_{eff}, surface gravity $\log g$, and projected rotational velocity $v \sin i$, from blue−violet optical spectra, as well as stellar mass M_*, stellar radius R_*, luminosity L_*, and visual-band extinction A_V from spectral energy distribution (SED) fitting, we also report approximate MK spectral types for all 104 bow shock stars based on visual inspection of spectra. We used the categorization scheme tabulated in the work of Z. Liu et al. (2019) and spectral peculiarities explained in A. Sota et al. (2011). Our spectral types are approximate and are not representative of the complexity of the full MK spectral

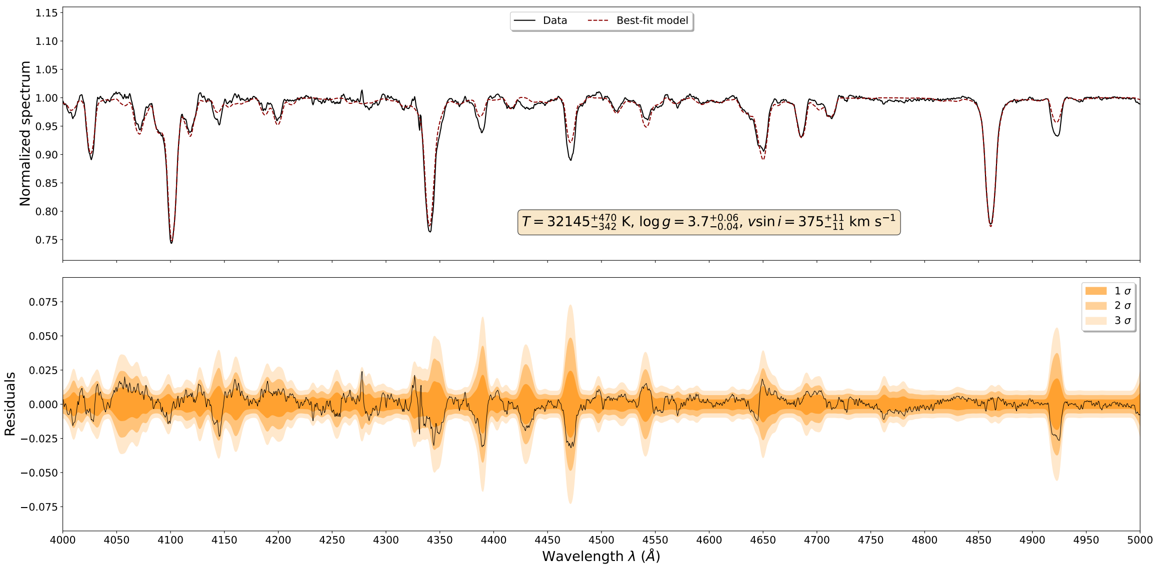

Figure 5. Top: observed spectrum (black) overplotted with best-fit, interpolated model (dashed red). Bottom: residual spectrum (black) with the uncertainties at each wavelength (orange).

classification scheme. We report them merely for comparison purposes. For more rigorous works on the MK classification of O and B stars, see A. Sota et al. (2011) and I. Negueruela et al. (2024).

3.4. Binarity Indicators

Due to the large multiplicity fraction of early-type stars (H. Sana & C. J. Evans 2011; R. Chini et al. 2012; H. A. Kobulnicky et al. 2014), we expect some fraction of bow shock stars to exhibit binarity. In this work we designate single-line spectroscopic binaries with the flag "SB1," as indicated by radial velocity variations exceeding those expected from a single star ($P_{\rm single} \leqslant 0.05$; H. A. Kobulnicky & W. T. Chick 2022).[13] We use "SB2" to flag double-lined spectroscopic binaries, as indicated either by line splitting in our spectra or spectra with unusual line ratios indicating composite spectra produced by two stars of different temperatures (i.e., strong He II lines in conjunction with Mg II features). We use "EB" to flag bow shock stars that are found to be eclipsing binaries in O. Y. Malkov et al. (2006). We flag probable astrometric binaries with "R," denoting a Gaia RUWE value >1.4.[14] In our analysis, we count stars with one or more of these flags as binaries. For probable binaries, we caution against taking the derived stellar parameters at face value, as our analysis is predicated on the assumption of one star. A detailed spectral decomposition analysis of composite spectra is infeasible for most of our targets given the low resolution and limited SNR.

3.5. Comparison Sample Results

3.5.1. Spectral Fitting Comparison

Table 3 presents this work's analysis on the comparison star sample. Alternating rows list literature results and measurements from this work, respectively. Column (1) lists the common identifier of the comparison star. Columns (2) and (3) are the R.A. and decl. in J2000 coordinates. Columns (4) and (5) report the temperature and its associated uncertainty. Columns (6) and (7) are the log surface gravity in cgs units and its uncertainty. Columns (8) and (9) are the projected rotational velocity and the uncertainty in this parameter. Column (10) is the reference for the measurement. For the purpose of comparison, we assume a temperature uncertainty of 1 kK, a gravity uncertainty of 0.10, and a rotational uncertainty of 10% when none is listed. We sometimes used two works for full stellar parameter comparisons. In this case, the first reference listed in the table was used for temperature and gravity information, while the second was used for projected rotational velocity.

Figure 6 plots our derived temperatures versus literature measurements (top panel) and the residuals from the 1:1 relation (bottom panel). The error bars in the bottom panel reflect uncertainties in literature measurements and this work added in quadrature. Since this work reports both upper and lower uncertainties on each measurement, the maximal error is used in the residual uncertainty calculation. The dashed black horizontal line illustrates zero deviation. Our results on temperature for the comparison sample agree to within 1σ of literature measurements across the entire sampled temperature range. Based on the residuals, we find that our derived temperatures scatter about literature values by 1.5 kK.

Figure 7 plots our measured values for gravity against literature values (top panel) and the residuals from the 1:1 relation (bottom panel). As in Figure 6, the error bars in the bottom panel reflect the quadrature sum of uncertainties from this work and those from the literature. Our results for gravity are generally in good agreement with literature measurements over the sampled gravity range with an rms of 0.20.

Figure 8 plots our rotational velocity against literature values (top panel) and the residuals from the 1:1 relation (bottom panel). Error bars are the same as in the previous two figures. Residuals are large and positive below the resolution limit 100 km s^{-1} and negative above this threshold. The instrumental resolution of KOSMOS of R 2200 corresponds to a velocity of approximately 100 km s^{-1}. Below the instrumental resolution, we conclude that we cannot reliably measure projected rotation. Above this limit, our

---

[13] This flag is only applicable for the subset of stars that are studied in both this work and H. A. Kobulnicky & W. T. Chick (2022).

[14] Due to the imprecision of astrometric solutions for bright stars, we exclude stars brighter than Gaia $B_P < 8$ mag from this criterion.

Table 3
Comparison Results

ID (1)	R.A. (2000) (HH:MM:SS) (2)	Decl. (2000) (°: :) (3)	T_{eff} (K) (4)	$\sigma_{T_{\mathrm{eff}}}$ (K) (5)	$\log g$ (6)	$\sigma_{\log g}$ (7)	$v \sin i$ (km s^{-1}) (8)	$\sigma_{v \sin i}$ (km s^{-1}) (9)	Reference(s) (10)
HD 36371	05:32:43.67	32:11:31.28	14600	300	2.11	0.06	36	5	W22
			16100	600	2.21	0.08	33	22	TW
HD 51309	06:56:08.22	−17:03:15.26	15600	400	2.59	0.05	30	6	W22
			17100	500	2.64	0.07	26	18	TW
HD 45418	06:27:00.88	−04:21:20.33	16800	130	4.27	0.04	247	8	M15
			15500	300	3.86	0.05	197	21	TW
HD 29309	04:38:15.23	31:59:55.64	16800	300	3.70	0.04	38	12	H10
			16400	600	3.55	0.08	41	30	TW
HD 47240	06:37:52.70	04:57:24.00	19500	…	2.47	…	111	…	S17
			22600	1100	2.93	0.11	101	23	TW
HD 35708	05:27:38.08	21:56:13.09	20700	200	4.15	0.07	25	2	N12
			19300	700	3.85	0.08	30	21	TW
HD 30677	04:50:03.61	08:24:28.24	21900	219	2.56	0.03	168	1	B23
			22200	800	2.92	0.07	147	15	TW
HD 202347	21:13:47.86	45:36:41.26	22600	125	3.77	0.04	95	5	M15
			21900	700	3.83	0.09	117	21	TW
HD 34989	05:21:43.56	08:25:42.80	24800	450	4.19	0.04	30	16	H10
			25800	1200	3.97	0.10	27	19	TW
BD +35 3956	20:05:59.98	35:45:44.42	24800	…	…	…	330	10	D07; H10
			23300	700	3.52	0.08	320	16	TW
HD 192660	20:14:26.08	40:19:45.05	25200	130	2.90	0.04	145	5	M15
			26300	1000	3.03	0.11	117	24	TW
HD 225146	00:03:57.50	61:06:13.09	28300	…	3.11	…	67	…	H22
			29000	800	3.37	0.12	102	20	TW
HD 47432	06:38:38.19	01:36:48.68	29100	…	3.04	…	97	…	H22
			28500	500	3.08	0.05	115	24	TW
HD 37128	05:36:12.81	−01:12:06.91	29500	…	3.22	…	55	…	S17
			26700	900	2.97	0.08	32	21	TW
HD 61347	07:38:16.12	−13:51:01.22	30900	…	3.12	…	112	…	S17
			32500	600	3.46	0.06	95	38	TW
HD 149757	16:37:09.54	−10:34:01.51	32000	…	3.66	…	385	…	H22
			32200	500	3.70	0.06	374	11	TW
HD 189957	20:01:00.00	42:00:30.82	32100	…	3.58	…	88	…	H22
			32400	400	3.54	0.06	100	15	TW
HD 191423	20:08:07.11	42:36:21.96	32300	…	3.71	…	397	18	H22; B23
			32400	600	3.54	0.07	409	20	TW
HD 225160	00:04:03.79	62:13:19.01	33200	…	3.35	…	77	…	H22
			33300	800	3.35	0.07	126	33	TW
HD 17603	02:51:47.80	57:02:54.47	33300	…	3.26	…	103	…	H22
			33300	900	3.34	0.07	147	28	TW
HD 34078	05:16:18.15	34:18:44.34	34500	…	4.07	…	13	…	H22
			33300	500	4.07	0.11	36	22	TW
HD 24431	03:55:38.42	52:38:28.75	34900	…	3.77	…	49	…	H22
			32900	800	3.77	0.11	97	22	TW
HD 41161	06:05:52.46	48:14:57.42	35200	…	3.84	…	331	…	H22
			35700	900	3.99	0.10	299	22	TW
HD 175876	18:58:10.77	−20:25:25.54	36100	…	3.59	…	282	…	H22
			37900	1600	3.75	0.11	258	26	TW
HD 5689	00:59:47.59	63:36:28.25	36800	…	3.72	…	255	…	H22
			38000	1100	3.81	0.08	223	17	TW
HD 36879	05:35:40.53	21:24:11.72	36900	…	3.77	…	209	…	H22
			36900	900	3.72	0.06	199	18	TW
HD 42088	06:09:39.57	20:29:15.45	40000	…	3.99	…	49	…	H22
			41200	1200	4.12	0.08	55	31	TW
BD +60 134	00:56:14.21	61:45:36.97	40700	…	3.95	…	234	9	H22; B23
			44800	1900	4.22	0.13	219	23	TW

Note. Column (1): common identifier for the comparison star. Column (2): R.A. of the comparison star in HH:MM:SS. Column (3): decl. of the comparison star in °: : . Column (4): temperature of the comparison star in units of K. Column (5): uncertainty in the reported temperature in units of K. Column (6): log surface gravity. Column (7): uncertainty in reported log surface gravity. Column (8): projected rotational velocity in units of km s^{-1}. Column (9): uncertainty in reported projected rotational velocity in km s^{-1}. Ellipses indicate no available information in the literature. Column (10): the shortened reference for the literature stellar parameter values. In the case of two references, the first reference was used for T_{eff} and $\log g$ and the second for $v \sin i$. Reference code: D07—S. Daflon et al. (2007); H10—W. Huang et al. (2010); N12—M. F. Nieva & N. Przybilla (2012); M15—J. M. Mugnes & C. Robert (2015); S17—S. Simón-Díaz et al. (2017); H22—G. Holgado et al. (2022); W22—D. Weßmayer et al. (2022); B23—N. Britavskiy et al. (2023); TW—this work.

(This table is available in machine-readable form in the online article.)

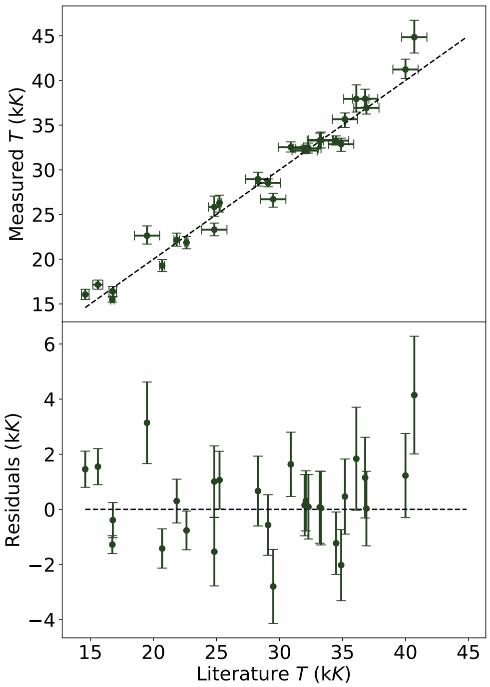

Figure 6. Temperature comparison between this work and values from the literature.

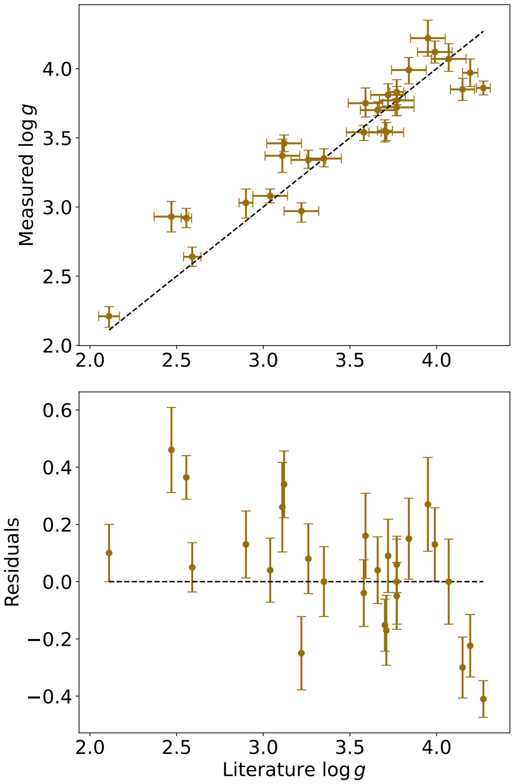

Figure 7. Gravity comparison between this work and values from the literature.

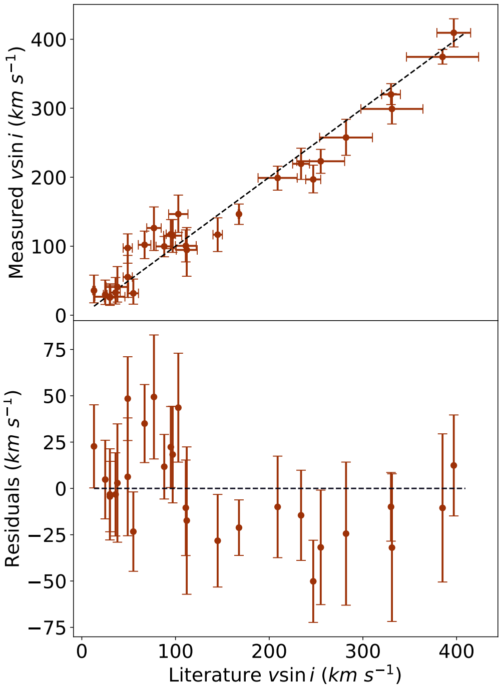

Figure 8. Projected rotational velocity comparison between this work and values from the literature.

measurements appear to be systematically smaller than literature values by approximately 25 km s^{-1}. We cannot explain this deviation. However, it is noteworthy that measurements appear to agree within 1σ, so we claim that our results serve as a reliable indicator of projected rotation, as our measurements are in agreement with the literature with an rms of 25 km s^{-1}, and our data are capable of identifying stars with rotational velocities exceeding 200 km s^{-1}.

3.5.2. Radius Comparison

From the results of the EXOFASTv2 analysis described in Section 3.2, we obtained stellar radii and provide comparisons to results from the literature. For ζ Oph (BS013) we obtain a stellar radius of $8.46^{+0.47}_{-0.43}\,R_\odot$. Our measurement is in good agreement with the value of 8.5 $R_\odot$ found in other works[15](A. Herrero et al. 1992; I. D. Howarth & K. C. Smith 2001; K. Shepard et al. 2022). For the comparison star HD 191423, we measure a stellar radius of $9.59^{+0.45}_{-0.43}\,R_\odot$, somewhat smaller than $18.3^{+8.7}_{-5.9}\,R_\odot$ as measured by L. Mahy et al. (2015), obtained from SED modeling. For V* AE Aur, which is a member of both our comparison sample and our bow shock sample (BS375), we obtain stellar radius $6.44^{+0.28}_{-0.26}$ $R_\odot$, in excellent agreement with the measurement of 6.8 0.5 $R_\odot$ from P. Aschenbrenner et al. (2023).

4. Properties of Bow Shock Stars

Table 4 lists the results of the analysis on the program stars. Column (1) gives the bow shock star identifier from the H. A. Kobulnicky et al. (2016) and T. Jayasinghe et al. (2019) catalogs. Column (2) gives the approximate MK spectral classification. We use the criteria developed in Z. Liu et al. (2019) to determine the approximate spectral type, with further qualifiers explained in A. Sota et al. (2011). For spectroscopic binaries, we report a classification of two O stars, an O star and a

---

[15] Other works (A. Herrero et al. 1992; I. D. Howarth & K. C. Smith 2001; K. Shepard et al. 2022) have noted the oblate shape of ζ Oph due to its near-critical rotation and can measure distinctly the polar and equatorial radii. We cannot distinguish these radii, and our measured value of 8.46 $R_\odot$ lies between measurements of polar radius of 7.0 $R_\odot$ and measurements of equatorial radius of 9.1 $R_\odot$.

B star, or two B stars, based on the presence and/or absence of He I and He II lines. Columns (3) and (4) give the measured temperature and uncertainty in temperature from spectra. Columns (5) and (6) list the measured $\log g$ and uncertainty from spectra. Columns (7) and (8) report the measured projected rotational velocity and its uncertainty, also measured from spectra. Typical uncertainties are 1000 K in temperature, 0.10 in $\log g$, and 40 km s^{-1} in $v \sin i$. Columns (9) and (10) report the stellar radius from EXOFASTv2 and its uncertainty. Columns (11) and (12) give the luminosity and uncertainty measured from EXOFASTv2. Lastly, columns (13) and (14) give the extinction in V band, A_V, and uncertainty, as measured in EXOFASTv2. For dubious bow shock star 2G3527642 + 0032660$_\star$, we exclude this star from analysis presented in this paper, and we list −99 to indicate null results on stellar parameters. See Appendix B for more discussion on this star.

4.1. Temperature

Figure 9 presents a histogram of retrieved temperatures for the bow shock stars in bins of 4000 K. We find temperatures ranging from 16,500 to 46,800 K, with a median value of 27,800 K. Defining a criterion of B stars having effective temperatures lower than 30 kK, we find that our sample of 103 OB program stars consists of 59 B stars (57%) and 44 O stars (43%). However, this should be not be interpreted as a true characterization of the parent sample given our magnitude-limited selection criteria.

4.2. Surface Gravity

Figure 10 presents the distribution of $\log g$ among the bow shock stars in bins of 0.25. We find log surface gravities ranging from 2.57 to 4.60, with a median value of 3.81. This is consistent with O- and B-type stars ranging in evolutionary stages from dwarf to supergiant.

4.3. Projected Rotational Velocity

Figure 11 presents the distribution of projected rotational velocity for the program stars in bins of 50 km s^{-1}. Due to the limitations of low-resolution spectrographs described in Section 2.2, a broadening of 100 km s^{-1} should be regarded as a floor, below which we cannot be certain of the projected rotational velocity. We find projected rotational velocities ranging from 18 to 375 km s^{-1}, with a median value of 100 km s^{-1}. A majority (52%) of program stars can be described as "slow rotators," with a projected rotational velocity below 120 km s^{-1}.

4.4. Binarity

We find that 62 bow shock stars (60% of the sample) show some indications of binarity. Of the total 104 bow shock stars, we find that 16 (15%) are single-lined spectroscopic binaries, 41 (39%) are double-lined spectroscopic binaries, 3 (3%) are eclipsing binaries, and 15 (14%) have Gaia RUWE > 1.4. Several bow shock stars show several indications of binarity, which is why the percentages add up to more than 100%. In the case of composite spectra (i.e., SB2) we expect the fitted spectral parameters to represent some average of both components of the system with larger uncertainties, in which a single-star model does not fit well. Our analysis is most problematic for deblended SB2s, in which $v \sin i$ is erroneously inflated to cover split lines.

4.5. Visual Extinction

H. A. Kobulnicky et al. (2016) presented K-band extinctions A_K for their sample of 709 stellar bow shock candidates based on the $H - [4.5]$ color-excess method described in S. R. Majewski et al. (2011). Using the J. A. Cardelli et al. (1989) extinction curve for average Galactic dust $R_V = 3.1$, we compute the corresponding A_V using the relation $A_V = 8.13 A_K$.

Figure 12 compares extinctions derived in this work using EXOFASTv2 (vertical axis) with transformed K-band extinctions from Rayleigh–Jeans color-excess (RJCE) methods (horizontal axis). Our extinctions derived from SED fitting are systematically higher than the RJCE extinctions in H. A. Kobulnicky et al. (2016). While there is a strong correlation between the two methods, the SED-fitting-derived extinctions are 2–3 mag larger than the RJCE values. The systematic difference between these two methods of measuring extinction indicates that the $H - [4.5]\,\mu$m color-excess technique is inappropriate for early-type stars, as noted by S. R. Majewski et al. (2011). The RJCE method described in S. R. Majewski et al. (2011) infers a K-band extinction from an $H - [4.5]\,\mu$m color. For spectral types A–M, S. R. Majewski et al. (2011) demonstrate that this color only varies by 0.1 mag. With the inclusion of B-type stars, this color varies by 0.4 mag. With the inclusion of O spectral types, this color trend may diverge as the atmospheres of stars become increasingly less affected by absorption from metals in the infrared spectrum with increasing temperature. We conclude that the SED-fitting techniques provide a more reliable measure of extinction than RJCE methods for early-type stars.

5. Discussion

5.1. Are Bow Shock Stars Distinct from Typical OB Stars?

Figure 13 plots $\log g$ versus $v \sin i$ for our sample of bow shock stars with no apparent indications of binarity (filled circles colored by stellar mass) and probable binary bow shock stars (gray triangles). For binary bow shock stars, we consider our measured $v \sin i$ to be an upper limit. Overlaid in the gray contours are the 16th-, 50th-, and 84th-percentile levels drawn from a sample of 285 Galactic O stars combined with 527 late O and early to mid-B supergiants studied in the IACOB project (G. Holgado et al. 2022; A. de Burgos et al. 2024). Colored tracks indicate maximum rotation rates, computed from the equation

$$v_{\rm crit} = \sqrt{\frac{GM_*}{R_*}(1 - \Gamma)}\,, \tag{3}$$

taking into account gravitational, Thompson scattering, and centrifugal accelerations, as derived in seminal works (N. Langer 1997, 1998; W. Glatzel 1998). The critical rotation relation in Equation (3) bears a resemblance to the escape velocity, and the two are related by $v_{\rm crit} = v_{\rm esc}/\sqrt{2}$. We choose Eddington Γ of 0.30, a value typical for OB stars (O. Verhamme et al. 2024). ζ Oph, a rapid rotator, lies to the right of the figure near its critical rotation track with a projected rotational velocity of 375 km s^{-1}. We measure a stellar mass of 15 $M_\odot$, corresponding to an estimated critical velocity of 450 km s^{-1}. Other works find a similar critical velocity of 500 km s^{-1} (K. Shepard et al. 2022). We find that bow shock stars occupy a similar locus of $\log g$ and $v \sin i$ as Galactic OB populations. With the exception of ζ Oph, the

Table 4
Bow Shock Star Results

ID (1)	Sp. T. (2)	$T_{\rm eff}$ (K) (3)	$\sigma_{T\,{\rm eff}}$ (K) (4)	$\log g$ (5)	$\sigma_{\log g}$ (6)	$v \sin i$ (km s^{-1}) (7)	$\sigma_{v \sin i}$ (km s^{-1}) (8)	R_* ($R_\odot$) (9)	σ_{R_*} ($R_\odot$) (10)	L_* ($L_\odot$) (11)	σ_{L_*} ($L_\odot$) (12)	A_V (mag) (13)	σ_{A_V} (mag) (14)	RUWE (15)	Flag (16)
$001_\star$	O+O e	34,100	2000	3.83	0.25	216	50	10.9	0.78	134,000	24,000	3.52	0.05	0.691	SB2
$007_\star$	B2–3 V	22,300	1500	4.44	0.18	58	40	3.57	0.2	2730	660	4.37	0.14	0.873	⋯
$010_\star$	B1 III	27,800	1500	3.81	0.16	43	26	8.03	0.51	27,700	5300	2.61	0.05	0.846	⋯
$013_\star$	O8–9 Vnn	32,200	500	3.70	0.06	375	11	8.46	0.47	65,500	8500	1.05	0.06	4.489	⋯
$016_\star$	O+B	27,400	1900	3.36	0.18	42	26	33.7	9.2	680,000	440,000	6.25	0.13	0.892	⋯
$019_\star$	B2–3 III	24,500	2000	3.48	0.25	47	32	35.4	10.0	520,000	340,000	6.26	0.10	0.815	⋯
$026_\star$	B+B	28,500	1000	3.90	0.16	417	45	15.29	0.99	144,000	24,000	5.14	0.05	0.815	SB2
$027_\star$	B5 III	22,500	1000	3.96	0.13	61	36	5.46	1.2	7300	4400	3.28	0.05	0.863	⋯
$039_\star$	O+B f	33,300	1300	3.38	0.13	87	50	30.0	6.7	1,010,000	540,000	6.07	0.16	0.845	SB2
$043_\star$	B2–3 I	26,900	1100	3.74	0.13	32	50	8.25	0.77	33,900	7500	3.77	0.04	1.968	R
$051_\star$	O+O	34,000	1000	4.41	0.21	52	58	10.9	1.7	125,000	37,000	6.27	0.07	1.032	SB2
$054_\star$	B1 III(n)	27,900	1200	3.01	0.11	138	53	18.3	1.2	125,000	19,000	2.67	0.04	0.758	SB1
$056_\star$	O+B	26,800	2000	3.71	0.24	52	35	28.8	6.0	440,000	230,000	5.33	0.07	1.864	SB2; R
$061_\star$	B0 III(n)	30,600	600	3.83	0.12	135	19	15.3	1.4	184,000	35,000	1.94	0.03	1.415	EB; R
$063_\star$	B+B	31,100	1100	4.21	0.21	92	33	7.08	0.42	39,100	5200	1.92	0.04	0.988	SB2
$064_\star$	O+B	46,500	2000	4.15	0.15	234	27	9.19	0.48	345,000	59,000	4.18	0.06	0.855	SB2
$065_\star$	B5 III(n)	21,200	700	3.72	0.09	91	50	6.22	0.31	6680	960	2.08	0.07	0.869	⋯
$066_\star$	O+O	41,300	3000	4.31	0.25	246	50	13.5	4.3	540,000	420,000	5.96	0.19	1.023	SB2
$067_\star$	O8–9 V	32,200	1200	4.15	0.21	42	27	8.54	0.5	70,300	11,000	4.87	0.08	1.002	⋯
$150_\star$	B1 V	25,100	1100	3.97	0.13	49	30	8.42	0.42	27,300	4300	5.25	0.11	1.657	R
$200_\star$	B2–3 I	25,100	1800	3.50	0.25	48	35	32.8	9.4	370,000	260,000	6.16	0.11	1.163	⋯
$240_\star$	B5 V	16,500	400	3.55	0.06	87	24	5.97	0.23	2250	260	2.45	0.05	0.855	⋯
$255_\star$	B2–3 V	20,000	800	3.71	0.10	33	20	6.17	0.29	5290	810	3.44	0.06	0.892	⋯
$288_\star$	B1 V(n)	27,200	1300	3.88	0.13	169	26	8.79	0.5	42,200	7500	2.86	0.04	0.880	⋯
$298_\star$	B1 1	22,400	1500	2.98	0.14	56	36	17.7	1.2	65,000	16,000	2.04	0.05	1.033	⋯
$300_\star$	B1 V	29,200	800	4.06	0.12	74	41	6.64	0.28	29,700	3500	2.73	0.05	0.835	⋯
$302_\star$	B2–3 V(n)	22,000	1000	3.79	0.14	211	40	8.54	0.67	16,700	3600	2.56	0.07	1.619	R
$303_\star$	B2–3 III	20,200	1600	2.70	0.18	45	31	68.4	22.0	790,000	570,000	5.99	0.19	0.987	SB1
$305_\star$	O+O	33,500	1000	4.59	0.15	269	45	10.2	1.5	119,000	41,000	3.12	0.11	5.203	SB1; SB2; R
$306_\star$	B+B	27,200	3000	3.58	0.23	218	55	9.61	0.7	53,000	17,000	2.86	0.08	0.970	SB2
$314_\star$	O+B	26,500	1400	3.69	0.15	210	28	12.4	1.5	71,000	24,000	2.17	0.11	0.987	SB2
$319_\star$	B+B	23,700	1300	3.08	0.15	47	30	35.6	4.1	424,000	120,000	4.17	0.05	0.957	SB1; SB2
$320_\star$	B1 I	27,800	1100	3.09	0.13	37	24	23.9	2.4	300,000	79,000	2.31	0.19	0.866	⋯
$321_\star$	B0 V(n)	30,900	1800	4.24	0.24	126	36	9.36	0.74	79,000	17,000	4.64	0.12	1.031	⋯
$322_\star$	O8–9 V	32,700	1000	3.98	0.17	100	24	13.96	0.95	206,000	34,000	5.03	0.08	1.045	SB1
$324_\star$	O+O	32,400	1000	4.01	0.15	207	26	17.3	1.3	306,000	54,000	3.39	0.05	0.893	SB2
$325_\star$	B2–3 III	21,600	800	3.29	0.10	33	20	15.35	0.82	47,100	7600	2.81	0.06	1.556	R
$326_\star$	B1 I	25,300	1700	3.71	0.29	61	45	21.0	1.4	196,000	45,000	4.33	0.06	1.077	⋯
$328_\star$	B+B	26,000	1500	3.97	0.23	158	62	9.6	0.61	390,000	7000	3.96	0.06	0.923	SB2
$330_\star$	B1 I	22,400	1000	2.94	0.12	42	27	28.4	1.4	177,000	28,000	3.60	0.05	1.041	⋯
$331_\star$	O+O	34,700	1000	3.92	0.13	192	20	16.9	0.43	68,800	7800	5.58	0.04	1.080	SB1; SB2
$332_\star$	O+O	32,200	800	3.95	0.13	199	22	8.64	0.43	68,800	7800	5.58	0.04	1.051	SB1; SB2
$335_\star$	B1 I	24,400	1200	3.32	0.14	52	29	16.99	0.77	82,500	9500	4.87	0.09	1.056	⋯
$339_\star$	O+O	45,600	4500	4.28	0.33	200	75	16.1	5.0	990,000	830,000	6.29	0.12	1.031	SB2
$340_\star$	B1 I	25,800	1200	3.42	0.12	29	20	11.24	0.56	48,000	7800	1.26	0.05	0.942	⋯
$341_\star$	O+O	33,100	800	4.32	0.16	150	23	13.4	2.8	196,000	93,000	6.16	0.09	1.301	SB1; SB2

Table 4
(Continued)

ID (1)	Sp. T. (2)	$T_{\rm eff}$ (K) (3)	$\sigma_{T\,{\rm eff}}$ (K) (4)	$\log g$ (5)	$\sigma_{\log g}$ (6)	$v \sin i$ (km s^{-1}) (7)	$\sigma_{v \sin i}$ (km s^{-1}) (8)	R_* ($R_\odot$) (9)	σ_{R*} ($R_\odot$) (10)	L_* ($L_\odot$) (11)	σ_{L*} ($L_\odot$) (12)	A_V (mag) (13)	σ_{AV} (mag) (14)	RUWE (15)	Flag (16)
343$_\star$	O+B	23,600	1500	2.57	0.18	96	50	54.3	3.0	820,000	140,000	3.55	0.04	0.897	SB2
344$_\star$	O6 If+	46,800	900	3.78	0.05	154	60	21.69	0.87	2,030,000	210,000	5.60	0.07	0.937	⋯
345$_\star$	B0 III	27,400	900	3.74	0.09	127	24	7.38	0.29	26,500	3300	2.53	0.06	0.874	⋯
346$_\star$	B1 III	21,400	1100	3.19	0.14	96	40	40.0	21.0	380,000	310,000	6.26	0.61	1.304	SB1
349$_\star$	O+B	25,200	1300	3.28	0.12	235	20	13.03	0.82	559,000	11,000	2.65	0.05	0.916	SB2; R
350$_\star$	B1 III	24,200	1600	3.16	0.17	91	40	35.8	8.2	450,000	270,000	5.14	0.07	3.800	SB1; R
351$_\star$	O8–9 III(n)	33,100	700	4.03	0.12	190	20	16.6	2.2	305,000	87,000	2.26	0.02	1.058	⋯
353$_\star$	O+B	37,700	1300	3.98	0.12	250	25	14.79	0.99	408,000	68,000	4.52	0.06	0.881	SB2
354$_\star$	O+B e	24,800	2400	2.93	0.21	448	74	38.5	5.0	530,000	220,000	4.76	0.20	0.996	SB2
356$_\star$	B1 III	26,200	1000	3.25	0.10	137	30	13.75	0.69	72,700	11,000	2.66	0.04	0.986	SB1
357$_\star$	B2–3 III	24,200	1000	3.24	0.10	113	30	18.1	2.0	98,000	28,000	2.74	0.04	3.035	SB1; R
358$_\star$	B5 III	20,500	700	3.83	0.08	45	30	4.27	0.16	2620	320	2.52	0.06	0.981	⋯
359$_\star$	B0 V	31,700	400	3.59	0.06	54	27	13.12	0.62	156,000	16,000	2.26	0.02	0.974	⋯
360$_\star$	B1 I	21,500	800	2.58	0.09	41	10	65.9	4.3	840,000	140,000	2.79	0.11	0.989	SB1
361$_\star$	B2–3 I	23,200	1800	2.69	0.17	51	20	44.3	3.0	609,000	100,000	4.62	0.03	1.046	SB1
362$_\star$	B+B	25,100	2100	3.34	0.21	237	38	15.2	1.1	105,000	27,000	5.54	0.06	1.153	SB2
364$_\star$	O7 V	34,600	600	4.37	0.12	77	24	9.06	0.72	106,000	19,000	1.87	0.03	2.220	R
365$_\star$	B1 III	26,800	1200	3.54	0.13	29	20	9.29	0.45	37,900	6200	2.24	0.08	0.913	⋯
366$_\star$	B0 V	30,200	400	4.02	0.05	89	20	18.04	1.0	248,000	32,000	0.89	0.04	1.014	⋯
367$_\star$	O8–9 V	32,500	900	3.95	0.15	52	30	11.6	0.54	138,000	17,000	4.25	0.04	1.140	⋯
368$_\star$	O+O	32,300	1000	3.91	0.17	308	30	9.26	0.5	84,300	11,000	4.17	0.04	1.246	SB2
369$_\star$	O7 V	37,300	1000	4.22	0.10	89	26	11.18	1.2	221,000	52,000	1.96	0.05	2.736	R
371$_\star$	O5 V	44,300	2500	4.23	0.18	120	46	8.97	0.69	272,000	69,000	3.96	0.04	1.294	SB1
372$_\star$	O8–9 V(n)	31,900	1000	3.93	0.15	142	26	12.22	0.87	143,000	24,000	3.84	0.07	1.107	SB1
373$_\star$	B5 III	23,700	500	3.73	0.06	33	21	5.94	0.28	9400	1200	0.58	0.04	1.178	⋯
374$_\star$	O+B	33,300	500	3.56	0.06	290	16	12.7	1.2	172,000	38,000	0.76	0.04	1.217	SB2
375$_\star$	O8–9 III	33,200	500	4.06	0.09	38	23	6.44	0.28	44,600	4400	1.80	0.06	0.993	⋯
376$_\star$	O+B	43,500	1600	4.04	0.11	185	27	11.03	0.75	386,000	75,000	1.00	0.10	0.949	SB2
377$_\star$	O+B	37,600	1100	3.97	0.09	104	29	9.93	0.46	170,000	22,000	1.97	0.02	0.930	SB2
378$_\star$	O8–9 V	32,700	500	4.19	0.08	39	21	5.94	0.42	36,700	5500	0.14	0.08	1.179	⋯
381$_\star$	O6 V	39,900	1200	4.03	0.10	107	23	13.9	1.3	450,000	95,000	1.34	0.13	1.105	⋯
383$_\star$	O+B f	34,300	600	3.31	0.05	145	43	26.9	2.2	890,000	170,000	2.33	0.04	1.033	SB2
384$_\star$	O+B	35,400	1500	4.26	0.22	246	42	12.53	0.77	229,000	37,000	3.10	0.06	0.973	SB 2
385$_\star$	O+B (f)	40,300	2100	3.81	0.11	227	22	12.68	0.67	356,000	69,000	3.33	0.03	0.985	SB2
386$_\star$	B1 I	24,500	1100	2.80	0.10	38	26	38.3	2.1	439,000	82,000	2.35	0.07	0.880	EB
388$_\star$	B2–3 I	21,800	1100	2.71	0.11	32	23	57.3	6.1	630,000	180,000	3.40	0.06	2.496	⋯
389$_\star$	B2–3 I	24,400	1000	3.31	0.10	28	19	15.65	1.0	71,000	13,000	2.39	0.04	1.383	⋯
634$_\star$	O8–9 V(n)	31,700	700	4.18	0.10	149	19	11.2	0.51	116,000	13,000	2.78	0.05	0.829	⋯
640$_\star$	O+B	27,300	1500	4.28	0.16	256	38	10.13	0.65	54,400	11,000	3.37	0.08	1.408	SB2; R
662$_\star$	O8–9 III(n)	32,800	900	3.81	0.13	154	19	13.42	0.8	187,000	27,000	1.56	0.07	0.816	⋯
667$_\star$	B0 III(n)	29,600	700	4.05	0.10	153	16	10.05	1.1	70,000	15,000	1.23	0.16	0.825	EB
673$_\star$	B1 V	27,100	1800	4.01	0.29	56	45	9.1	1.8	37,500	18,000	5.49	0.37	1.375	⋯
687$_\star$	B+B	27,100	2100	4.19	0.35	261	130	19.6	9.9	190,000	210,000	6.31	0.28	1.028	SB2
692$_\star$	O+O	36,800	1100	4.60	0.14	110	51	10.62	0.52	190,000	24,000	5.21	0.03	1.055	SB2
700$_\star$	B+B	27,000	1900	3.82	0.25	158	79	25.0	11.0	420,000	340,000	6.29	0.37	0.884	SB2
705$_\star$	B1 III	27,100	1500	3.45	0.16	132	51	14.8	0.9	109,000	22,000	3.99	0.07	0.944	⋯

Table 4
(Continued)

ID (1)	Sp. T. (2)	$T_{\rm eff}$ (K) (3)	$\sigma_{T\,{\rm eff}}$ (K) (4)	$\log g$ (5)	$\sigma_{\log g}$ (6)	$v \sin i$ (km s^{-1}) (7)	$\sigma_{v \sin i}$ (km s^{-1}) (8)	R_* ($R_\odot$) (9)	σ_{R*} ($R_\odot$) (10)	L_* ($L_\odot$) (11)	σ_{L*} ($L_\odot$) (12)	A_V (mag) (13)	σ_{A_V} (mag) (14)	RUWE (15)	Flag (16)
2G0063185-0066622$_\star$	B+B	24,000	1600	3.04	0.19	46	36	43.0	11.0	58,000	380,000	6.23	0.13	0.874	SB2
2G0065094-0061344$_\star$	B+B	27,900	1700	3.71	0.18	217	35	7.35	0.49	28,100	6500	4.73	0.07	1.303	SB2
2G0118310-0062990$_\star$	B2–3 III	23,000	800	3.43	0.10	30	21	11.51	0.59	31,400	4900	1.70	0.05	0.885	⋯
2G0592097+0012519$_\star$	B+B	26,200	2000	3.69	0.24	190	54	29.5	10.0	420,000	350,000	6.36	0.15	2.037	SB2; R
2G0600615-0018340$_\star$	B0 V	29,800	700	3.96	0.12	151	17	8.18	0.37	49,000	5200	3.00	0.04	0.847	⋯
2G0770694+0193568$_\star$	B0 V	30,100	600	4.03	0.09	103	20	7.24	0.55	39,400	6700	2.27	0.04	3.412	R
2G1045666+0128085$_\star$	O+B	34,900	500	4.64	0.11	243	30	11.42	0.51	176,000	51,000	3.01	0.05	1.069	SB2
κ Cas	B1 I	22,800	1200	2.72	0.11	33	23	81.1	7.4	1,740,000	430,000	1.13	0.10	2.368	⋯
2G3525610+0001887$_\star$	B+B	26,700	1700	3.77	0.19	129	54	10.58	0.71	56,000	13,000	4.75	0.10	1.021	SB2
2G3527642+0032660$_\star$	F	−99	−99	−99	−99	−99	−99	−99	−99	−99	−99	−99	−99	0.923	⋯
2G3533026+0008095$_\star$	O+B	39,600	1800	3.97	0.14	209	22	13.86	0.73	435,000	73,000	4.48	0.04	0.921	SB2
2G3585210+0089852$_\star$	O+B	34,700	500	4.44	0.13	181	19	11.14	0.75	164,000	24,000	5.08	0.07	0.930	SB2

Note. Column (1): stellar bow shock nebulae identifier from H. A. Kobulnicky et al. (2016) and addendum T. Jayasinghe et al. (2019) catalogs. Column (2): approximate MK spectral type. Column (3): measured $T_{\rm eff}$ in K. Column (4): uncertainty on $T_{\rm eff}$ in K. Column (5): measured $\log g$. Column (6): uncertainty on $\log g$. Column (7): measured $v \sin i$ in km s^{-1}. Column (8): uncertainty on $v \sin i$ in km s^{-1}. Column (9): stellar radius in $R_\odot$. Column (10): uncertainty on stellar radius in $R_\odot$. Column (11): luminosity in $L_\odot$. Column (12): uncertainty on luminosity in $L_\odot$. Column (13): visual-band extinction in magnitudes. Column (14): uncertainty on A_V in magnitudes. Column (15): Gaia RUWE value. Column (16): binary flag. Key: SB1—probability of single star < 0.05, as found in W. T. Chick et al. (2020); SB2—double-line spectroscopic binary; EB—eclipsing binary in O. Y. Malkov et al. (2006); R—Gaia RUWE > 1.4; ellipses—no apparent indicators of binarity.

(This table is available in machine-readable form in the online article.)

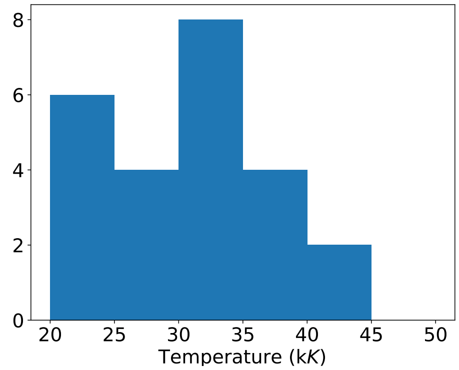

Figure 9. Temperature distribution of bow shock stars.

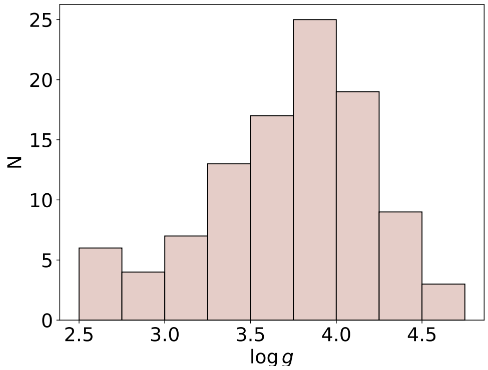

Figure 10. $\log g$ distribution of bow shock stars.

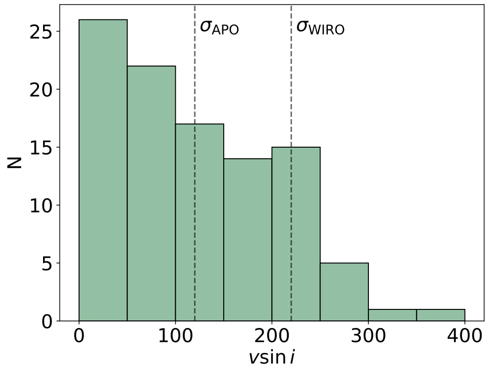

Figure 11. Projected rotational velocity distribution of bow shock stars.

bow shock sample does not contain any stars close to the critical rotational velocity. A handful of bow shock stars lie above $\log g \geqslant 4.40$ in a region not shared by `IACOB` stars, but these are almost exclusively probable binaries. The four bow shock stars displaced to the right of the panel are also probable binaries, with high measured rotational velocities due to the increased line width from the blended motions of two stars, which compromises the $v \sin i$ measurement.

Figure 14 presents a spectroscopic H-R diagram[16] (panel (a)) and a conventional H-R diagram (panel (b)) using luminosities derived from SED modeling. Solid diagonal tracks denote lines of constant gravity in the spectroscopic H-R diagram (panel (a)) and constant radius in the conventional H-R diagram (panel (b)). Bow shock stars that do not show apparent indications of binarity are colored by $\log g$ in both panels, and probable binary bow shock stars are represented in gray. MIST stellar tracks (J. Choi et al. 2016), computed with zero rotation and solar metallicity, are overplotted for a range of stellar masses in both panels in dashed gray lines. In the spectroscopic H-R diagram (panel (a)), we expect binary bow shock stars, especially deblended SB2s, to not be in concordance with stellar models, as retrieved stellar parameters for these systems are questionable. In the conventional H-R diagram (panel (b)), we expect the binary bow shock stellar luminosity to be the fitted luminosity of both components of the binary system.

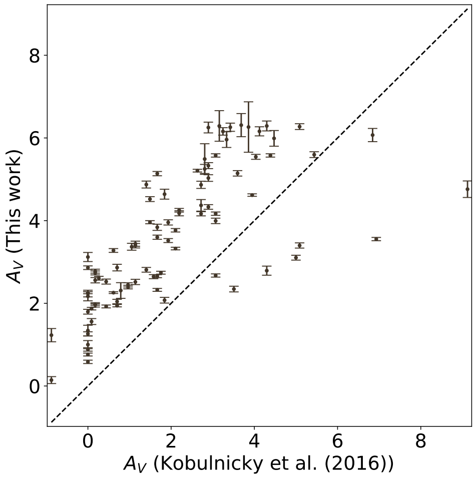

Figure 12. Visual-band extinction compared with transformed extinctions from previous work.

In the spectroscopic H-R diagram (panel (a)), we find that bow shock stars show good agreement with evolutionary models for masses ranging from 6 to 80 $M_\odot$. Many of them fall along the main sequence. Three high-$\log g$ stars stand out conspicuously in the spectroscopic H-R diagram, below the zero-age main sequence (ZAMS), just above 30 kK and between the 12 and 20 $M_\odot$ models. These were flagged as being possible binaries.

In the conventional H-R diagram (panel (b)), we again find that bow shock stars agree with evolutionary models with masses ranging from 6 to 80 $M_\odot$. The low-mass, high-$\log g$ star in the lower right corner of the spectroscopic H-R diagram appears in a similar location to that in the top panel and lies between the 6 and 8 $M_\odot$ tracks. The bow shock stars occupy the same locus on the top panel as on the bottom panel, demonstrating the agreement between these two different luminosity indicators. In the bottom panel, high-$\log g$ stars cluster near the ZAMS, while low-$\log g$ stars scatter to the right. This is an expected result, as main-sequence stars have smaller radii at a given stellar mass than evolved stars. Probable binaries have larger mean uncertainties on luminosity in both panels, as a result of the larger uncertainty on temperature in the spectral fitting. Larger temperature uncertainties propagate to the EXOFAST fitting, yielding large uncertainties in measure luminosity.

5.2. Are Bow Shock Stars Runaways?

The formation mechanism of runaway stars is an active area of research. The two most prominent mechanisms are the

---

[16] The spectroscopic H-R diagram (N. Langer & R. P. Kudritzki 2014) plots spectroscopic luminosity $\mathcal{L}$, defined as $\mathcal{L} = T_*^4/g \propto L_*/M_*$. The spectroscopic H-R diagram is useful because it does not rely on a parallax or radius measurement and only requires stellar parameters obtained from spectra.

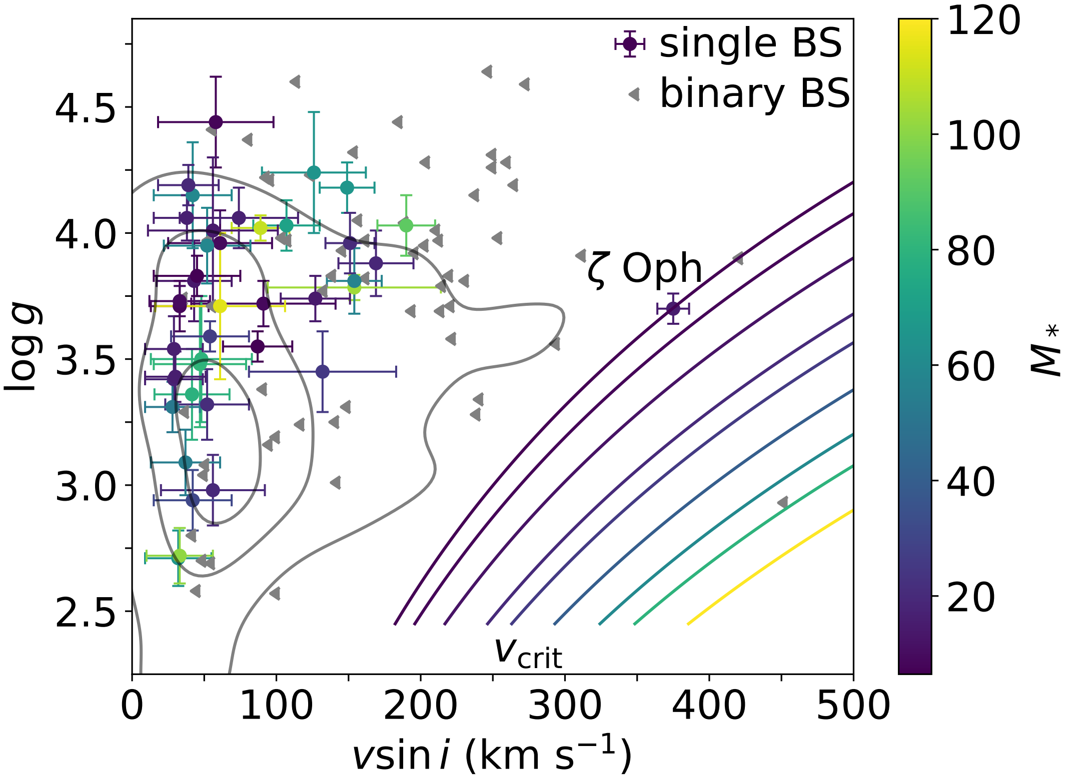

Figure 13. $\log g$ vs. $v\sin i$ for single bow shock stars (colored points), binary bow shock stars (gray triangles), and 16th/50th/84th-percentile levels for stars drawn from the IACOB sample. The colored tracks show theoretical maximum rotational velocities for a range of masses indicated by the color bar, with an Eddington factor $\Gamma = 0.30$ (solid colored tracks).

binary supernova scenario (BSS; F. Zwicky 1957; A. Blaauw 1961; J. Boersma 1961) and the dynamical ejection scenario (DES; A. Poveda et al. 1967; P. J. T. Leonard 1991). Some works propose a two-step mechanism in which both processes act on the same system when a dynamically ejected binary receives an additional kick as the primary undergoes a supernova (J. Pflamm-Altenburg & P. Kroupa 2010; J. Dorigo Jones et al. 2020). In the BSS, the process of mass transfer from the primary to the secondary will spin up and deposit nuclear-processed material onto the secondary. With the reversal of the mass ratio, it is then expected that the orbit will widen presupernova. The BSS will thus produce "walk-away" stars with high rotational velocities. M. Renzo et al. (2019) find, for example, a 90th-percentile peculiar velocity of 20 km s^{-1} and that the mean runaway velocity of the secondary is largely independent of the parameters of the progenitor system. Interestingly, the BSS is thought to produce bound systems with the asymmetry in the SN explosions providing a kick to the entire system. In their simulations, M. Renzo et al. (2019) find that 14% of systems modeled resulted in an MS–compact object bound system. Such systems are thought to be the origin of high-mass X-ray binaries (HMXBs; J. R. Gott 1971; C. T. Bolton 1972; E. P. J. van den Heuvel & J. Heise 1972; B. L. Webster & P. Murdin 1972). G. D. Phillips et al. (2024) proposed that mass transfer preceding the supernova of the primary is the source of Oe and Be stars, with the enhanced rotation creating a circumstellar decretion disk as the star surpasses its critical rotational velocity. The DES, on the other hand, is the process in which N-body interactions between massive stars and binary–binary interactions eject stars out of a natal cluster. The DES will leave its signature on the peculiar motions of the newly created runaway stars, with simulations finding binary–binary interactions creating runaways with speeds of the order of 100 km s^{-1} (A. Poveda et al. 1967), with no enhancement on rotational velocity. Previous works have searched for indications of both processes to ascertain the prominence of each channel in the formation of runaways. R. Hoogerwerf et al. (2000) used proper-motion data of nearby runaway stars and pulsars as indicators of the BSS and DES contributing to the production of runaways. They concluded that the high-proper-motion stars AE Aur and μ Columbae are likely to be products of the DES. Conversely, ζ Oph is a likely product of the BSS, traced back to a common locus in a young stellar group with oppositely directed, high-proper-motion pulsar J1932+1059. We expect to find two distinguishable runaway populations: BSS products with high projected rotational velocities and modest peculiar space velocities, and DES products with low projected rotational velocities and high peculiar space velocities.

Figure 15 plots our projected rotational velocities against the 2D peculiar space velocities, from H. A. Kobulnicky & W. T. Chick (2022), for bow shock stars. Single bow shock stars are colored by their measured $\log g$ and have error bars. Bow shock stars with indications of binarity are represented with gray triangles. For these systems, we expect the retrieved $v\sin i$ to represent an upper limit. We divided the plot into five regions: a low-velocity, nonrunaway region with $v_{\rm 2D} < 25$ km s^{-1} (purple infill), the BSS region with projected rotational velocities $v\sin i > 120$ km s^{-1} (well above the resolution limits of WIRO and KOSMOS spectrographs) and runaway velocity 25 km s^{-1} $< v_{\rm 2D} < 40$ km s^{-1} (yellow), the ambiguous runaway region with modest $v\sin i < 120$ km s^{-1} and 25 km s^{-1} $< v_{\rm 2D} < 40$ km s^{-1} (blue), the DES region

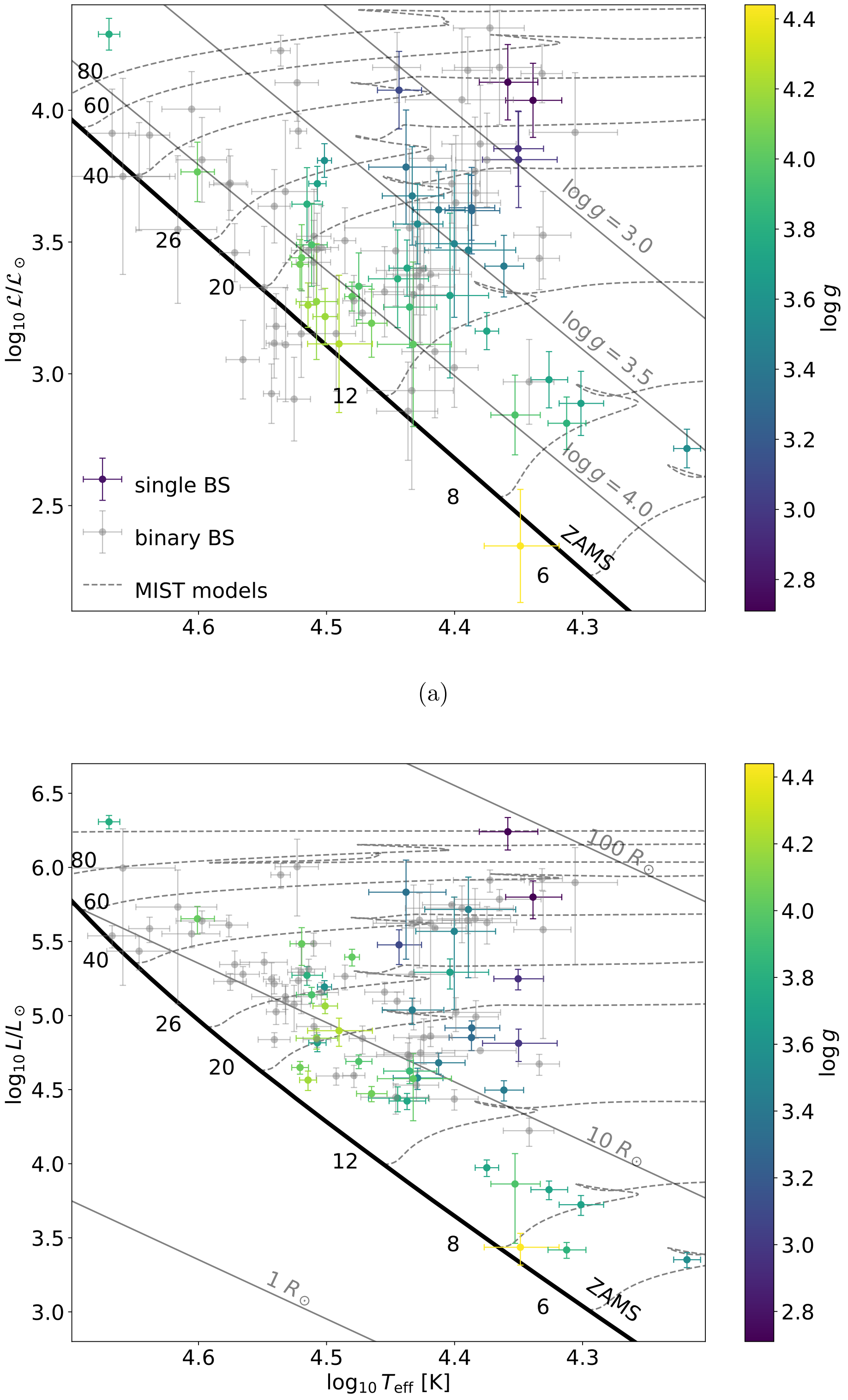

(a)

(b)

Figure 14. (a) Spectroscopic and (b) conventional H-R diagrams for bow shock stars. Bow shock stars without apparent indications of binarity are color-coded according to their measured $\log g$. Bow shock stars with indications of binarity are colored in gray. MIST evolutionary models are plotted with dashed lines, with ZAMS masses labeled.

with $v \sin i < 120 \text{ km s}^{-1}$ and $v_{2D} > 40 \text{ km s}^{-1}$ (cyan), and an avoidance region (as noticed in H. Sana et al. 2022; Y. Guo et al. 2024) with $v \sin i > 120 \text{ km s}^{-1}$ and $v_{2D} > 40 \text{ km s}^{-1}$ (peach). We find that 19 of the 87 OB stars with kinematic data (22%) are runaways under this criterion, consistent with the measured runaway fraction for OB stars measured in other studies (A. Blaauw 1961; R. C. Stone 1979; D. R. Gies & C. T. Bolton 1986; J. B. Lamb et al. 2016).

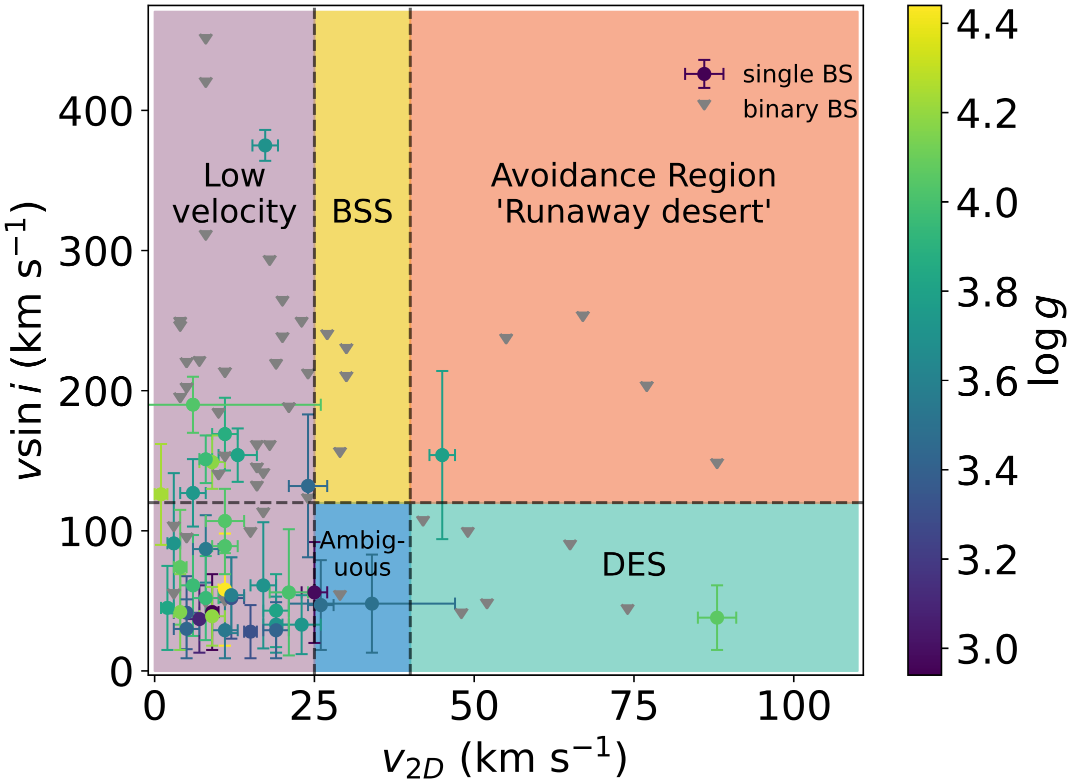

Figure 15. $v \sin i$–peculiar space velocity distribution for bow shock stars. Single bow shock stars are colored by measured log g, and binary bow shock stars are represented by gray triangles.

In the yellow BSS region there are four bow shock stars (BS324$_\star$, BS362$_\star$, BS385$_\star$, and BS667$_\star$), the first three of which present as double-lined spectroscopic binaries. The fact that we find an abundance of double-lined spectroscopic binaries in the BSS region is not surprising, considering that blended spectra of two stars will be interpreted erroneously as rapid rotators. BS667$_\star$ (V1202 Sco) is a well-known eclipsing binary star (O. Y. Malkov et al. 2006; E. A. Avvakumova et al. 2013; S. N. Mellon et al. 2019) and very likely is not rotating at the indicated $v \sin i$ of 150 km s^{-1}. In all likelihood, this star would be seen as a double-lined spectroscopic binary at higher spectral resolution. All four of the objects in this quadrant show indications of binarity. Therefore, the indicated $v \sin i$ in this region can be regarded as an upper limit, and none of these objects are likely to be rapid rotators.

In the blue ambiguous region there are three stars (BS019$_\star$, BS200$_\star$, and BS361$_\star$), with BS361$_\star$ being classified as a single-lined spectroscopic binary. These stars are interpreted as either BSS stars with diminished projected rotational velocities due to the orientation of the star's rotational axis or DES stars ejected with a velocity vector only partially in the plane of the sky.

In the cyan DES region of the plot there are seven stars (BS039$_\star$, BS303$_\star$, BS343$_\star$, BS360$_\star$, BS375$_\star$, BS377$_\star$, and BS386$_\star$), with BS039$_\star$, BS343$_\star$, and BS377$_\star$ classified as double-lined spectroscopic binaries and BS303$_\star$ and BS360$_\star$ categorized as single-lined spectroscopic binaries. BS375$_\star$ (AE Aur), an O8–9 III, is classified as a DES product in this work, consistent with the conclusions of R. Hoogerwerf et al. (2000). BS386$_\star$ (B1 I) was determined to be a strong candidate for the BSS in L. Kaper et al. (1997) on the basis of being a component of an HMXB system. It may fall into the DES region rather than the BSS region either because the star is viewed at low inclination or because the previously large rotation velocity diminished during its evolution into a supergiant. Alternatively, this object could be a member of a composite class of systems in which a binary ejected by N-body encounter subsequently receives an additional kick when the primary undergoes a supernova.

Five bow shock stars (BS064$_\star$, BS339$_\star$, BS344$_\star$, BS353$_\star$, and BS383$_\star$) fall into the peach avoidance region, with BS064$_\star$, BS339$_\star$, BS353$_\star$, and BS383$_\star$ classified as double-lined spectroscopic binaries. Given that these are erroneously classified as rapid rotators, it is reasonable that these four objects are actually runaway binary systems with lower rotational velocities. As for BS344$_\star$ (O6 If+), more commonly known as BD +43 3654, we find a best-fit $v \sin i$ of 145 43 km s^{-1}, straddling the boundary of the DES and avoidance region. Other works (V. V. Gvaramadze & A. Gualandris 2011; M. Carretero-Castrillo et al. 2023) determine N-body encounters to be the origin of this star's excessive peculiar velocity. Given these results and the imprecision in our measured $v \sin i$, we conclude that BS344$_\star$ should, in all likelihood, reside in the DES region.

Of the 19 bow shock stars that we deem as runaways, 15 show indications of binarity, suggesting a high incidence of binary bow shock runaways (⩾79%). While both the BSS and DES mechanisms are thought to produce runaway bound systems, the efficiency of producing these systems varies. In their simulations, M. Renzo et al. (2019) find that of the stars that do not merge, 14% of BSS systems remain bound after supernova of the primary, while H. B. Perets & L. Šubr (2012) find the DES to produce runaways with a multiplicity fraction between 20% and 45%. Given the abnormally high incidence of binarity in our sample of bow shock runaways, we consider this an indication of the DES being the preferred channel in producing runaway bow shock stars, and possibly runaway OB stars in general.

6. Conclusions

We have collected 104 low-resolution blue spectra of bow-shock-powering stars and measured best-fitting temperatures, gravities, and projected rotational velocities for the subsample of 103 OB stars. We have also obtained 28 spectra for a sample of well-studied comparison OB stars and have shown that our analysis reproduces literature measurements of those stellar parameters. Archival optical and near-IR photometry provides constraints on additional stellar parameters radius, mass, luminosity, and visual extinction, to fully characterize the bow shock stars.

Bow shock stars span a range of temperatures from 16.5 to 46.7 kK, $\log g$ from 2.50 to 4.60, and projected rotational velocities $<$100–400 km s^{-1}, which are typical ranges of Galactic OB stars. Notably, none of the bow shock stars have temperatures less than 16 kK (excluding 2G3527642 +0032660, an F dwarf that was erroneously selected as a candidate central star). Bow shock stars are unexceptional in their placement on both the spectroscopic and conventional H-R diagrams. We determine that 22% of bow shock stars with kinematic data (19 of 84) are runaways, based on their two-dimensional peculiar space velocity ($v_{2D} > 25$ km s^{-1}), consistent with other OB populations. We find that 65 (60%) of the bow shock stars show evidence of binarity. The high incidence of binary stars in runaway bow shock systems (15 of 19, $\geqslant$79%) indicates that the DES is the preferred mechanism for creating bow shock runaways, and possibly OB runaways in general. With the exception of ζ Oph, no bow shock stars rotate at or near breakup speeds.

These basic data provide secure fundamental stellar parameters for 103 OB bow shock stars, in many cases for the first time. These basic data will inform future use of this sample to measure mass-loss rates $\dot{M}$ in the same manner as H. A. Kobulnicky et al. (2018, 2019). Given our findings on runaway bow shock stars, we recommend that future works investigate the characteristics of dynamically ejected and binary supernova-ejected systems, namely binarity, rotation rates, and peculiar space velocities for these populations.

Acknowledgments

This work has been funded by NSF through grants AST-2108347, AST-1852289, and AST-2108349.

Facilities: ARC, WIRO.

Software: IRAF (National Optical Astronomy Observatories 1999), EXOFASTv2: Generalized publication-quality exoplanet modeling code .

Appendix A
Normalized Spectra

Figure 16 presents vertically stacked, normalized spectra for each bow shock star observed in this study in the wavelength range 4000–5000 Å, organized by bow shock identifier number up to BS709, then by Galactic longitude for the T. Jayasinghe et al. (2019) objects. The complete figure set (15 images) is available in the online journal. We label characteristic absorption and emission features with their source atom and ionization state and the approximate central wavelength in angstroms, in a similar style to the Galactic O-Star Spectroscopic Survey (A. Sota et al. 2011). Balmer lines (top) and DIBs (bottom) are colored in black, neutral and singly ionized helium (top) in red, silicon (bottom) in all ionizations in yellow/orange, and carbon/nitrogen/oxygen (top) in green. Trends in absorption strengths across temperature and surface gravities are often degenerate; however, for O and B stars, helium generally indicates temperature and silicon luminosity.

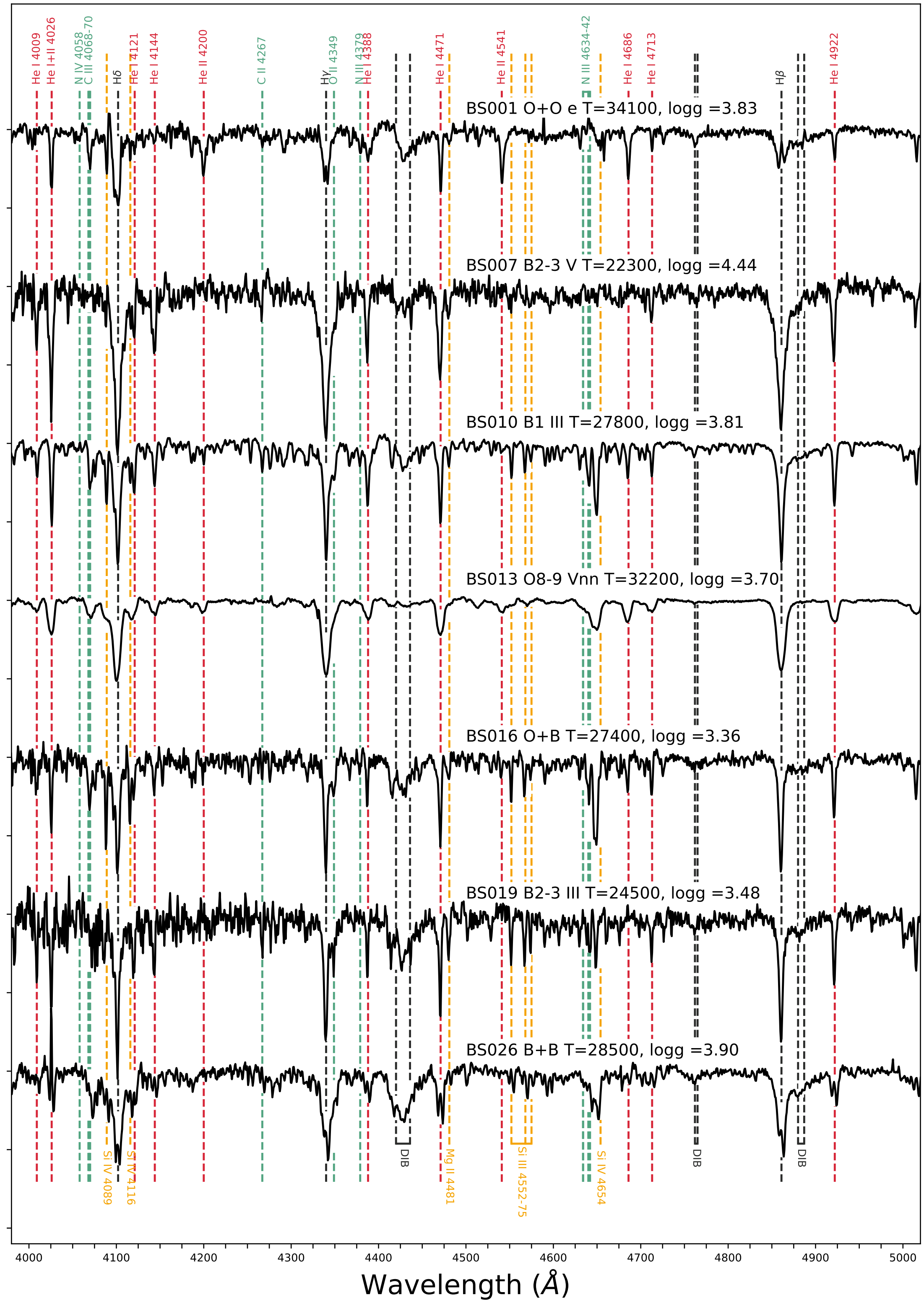

Figure 16. Bow shock stellar spectra.
(The complete figure set (15 images) is available in the online article.)

Appendix B
2G3527642+0032660 (HD 157642)

The curious bow-shock-powering candidate star 2G3527642+0032660 in T. Jayasinghe et al. (2019) (HD 157642, at a distance of 175 pc) may be a mistaken central star. HD 157642 is a bright star, with a spectral type F5–F8 (N. Houk 1982; A. J. Cannon & E. C. Pickering 1993). Our spectrum confirms this classification (based on the detection of Fe I λλ4046, 4383 and Ca I λ4226 features). It is likely therefore that another nearby star (or different physical phenomenon) is the source of the nebular emission surrounding HD 157642.

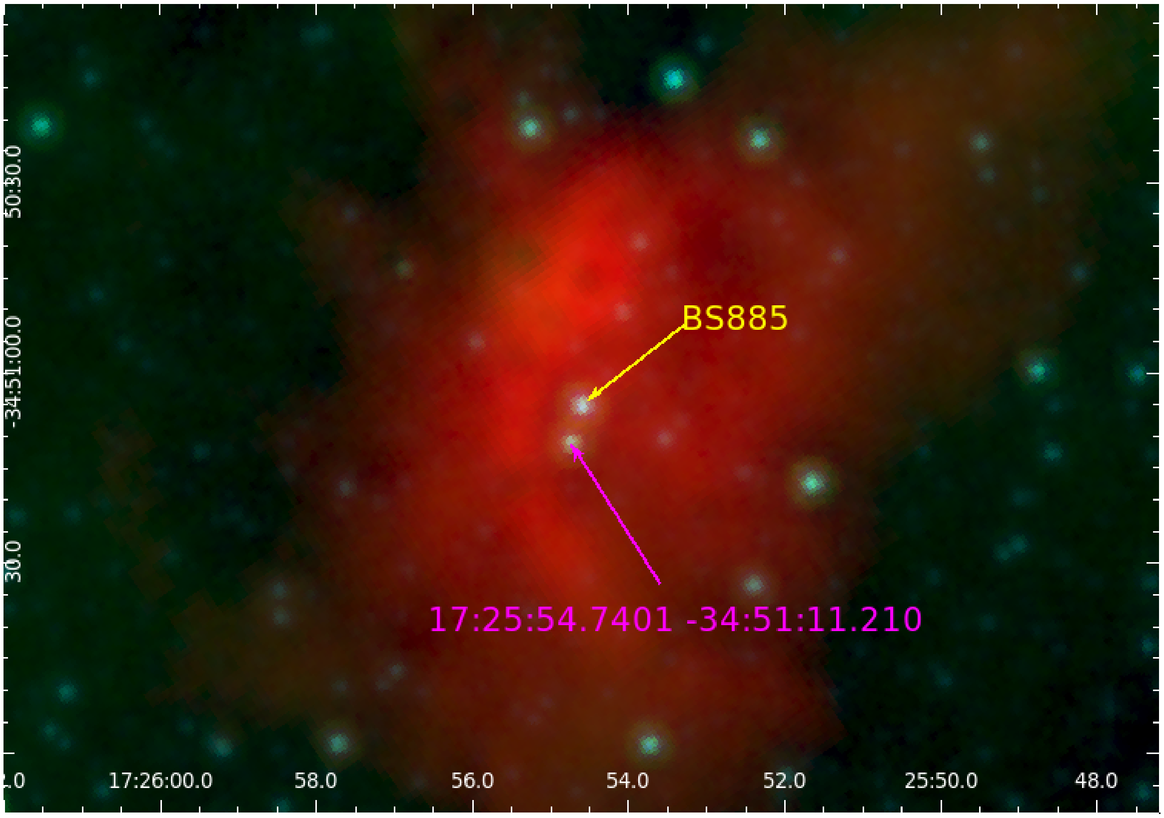

Figure 17. SST image of HD 157642 (object 2G3527642+0032660 in the T. Jayasinghe et al. 2019 catalog), with red/green/blue representing 24/8.0/4.5 μm data.

Figure 17 presents the IR bow shock nebula surrounding HD 157642 using archival SST data, with red/green/blue illustrating 24/8.0/4.5 μm data, using the IPAC SST data explorer (P. Capak 2019). The yellow arrow indicates HD 157642 (internal identification BS885), and the magenta arrow indicates the position of a nearby 4.5 μm source. There is no Gaia source ID for this other source, suggesting that it is heavily extincted. It is possible therefore, assuming that the nebula is indeed a stellar bow shock, that the heavily attenuated star could be the driving source of the bow shock nebulae and 2G3527642 + 0032660$_\star$ is a foreground F5V star coincidentally along the axis of symmetry of the bow shock nebula.

ORCID iDs

Nikhil Patten https://orcid.org/0009-0005-0582-8469
Henry A. Kobulnicky https://orcid.org/0000-0002-4475-4176
Matthew S. Povich https://orcid.org/0000-0001-9062-3583
Angelica S. Whisnant https://orcid.org/0000-0003-1963-5754
Alexandra Boone https://orcid.org/0009-0006-3467-630X
Srujan Dandu https://orcid.org/0000-0003-4578-3216
S. Nick Justice https://orcid.org/0009-0007-6290-3319
Alexander Larsen https://orcid.org/0000-0002-2401-8411
Ryan McCrory https://orcid.org/0009-0005-1158-6777
Maria Renee Meza https://orcid.org/0009-0002-8615-6403
Alexandra C. Rosenthal https://orcid.org/0009-0001-2223-2975
Noshin Yesmin https://orcid.org/0009-0009-4618-8049
Daniel A. Dale https://orcid.org/0000-0002-5782-9093

References

Abbott, B. P., Abbott, R., Adhikari, R., et al. 2009, RPPh, 72, 076901
Abbott, D. C., Bieging, J. H., Churchwell, E., & Cassinelli, J. P. 1980, ApJ, 238, 196
Arun, K. G., Belgacem, E., Benkel, R., et al. 2022, LRR, 25, 4
Aschenbrenner, P., Przybilla, N., & Butler, K. 2023, A&A, 671, A36
Avvakumova, E. A., Malkov, O. Y., & Kniazev, A. Y. 2013, AN, 334, 860
Bally, J., Heathcote, S., Reipurth, B., et al. 2002, AJ, 123, 2627
Benaglia, P., Vink, J. S., Martí, J., et al. 2007, A&A, 467, 1265
Björklund, R., Sundqvist, J. O., Puls, J., & Najarro, F. 2021, A&A, 648, A36
Björklund, R., Sundqvist, J. O., Singh, S. M., Puls, J., & Najarro, F. 2023, A&A, 676, A109
Blaauw, A. 1961, BAN, 15, 265
Boersma, J. 1961, BAN, 15, 291
Bolton, C. T. 1972, Natur, 235, 271
Bradaschia, C., Del Fabbro, R., Di Virgilio, A., et al. 1990, NIMPA, 289, 518
Britavskiy, N., Simón-Díaz, S., Holgado, G., et al. 2023, A&A, 672, A22
Cannon, A. J., & Pickering, E. C. 1993, yCat, 3135, 0
Capak, P. 2019, Spitzer Enhanced Imaging Products (SEIP) Source List, IPAC, doi:10.26131/IRSA3
Cardelli, J. A., Clayton, G. C., & Mathis, J. S. 1989, ApJ, 345, 245
Carneiro, L. P., Puls, J., Sundqvist, J. O., & Hoffmann, T. L. 2016, A&A, 590, A88
Carretero-Castrillo, M., Ribó, M., & Paredes, J. M. 2023, A&A, 679, A109
Chick, W. T., Kobulnicky, H. A., Schurhammer, D. P., et al. 2020, ApJS, 251, 29
Chini, R., Hoffmeister, V. H., Nasseri, A., Stahl, O., & Zinnecker, H. 2012, MNRAS, 424, 1925
Choi, J., Dotter, A., Conroy, C., et al. 2016, ApJ, 823, 102
Czekala, I., Andrews, S. M., Mandel, K. S., Hogg, D. W., & Green, G. M. 2015, ApJ, 812, 128
Daflon, S., Cunha, K., de Araújo, F. X., Wolff, S., & Przybilla, N. 2007, AJ, 134, 1570
Dahlem, M., Petr, M. G., Lehnert, M. D., Heckman, T. M., & Ehle, M. 1997, A&A, 320, 731
de Burgos, A., Simón-Díaz, S., Urbaneja, M. A., & Puls, J. 2024, A&A, 687, A228

de Mink, S. E., Langer, N., Izzard, R. G., Sana, H., & de Koter, A. 2013, ApJ, 764, 166

Dorigo Jones, J., Oey, M. S., Paggeot, K., Castro, N., & Moe, M. 2020, ApJ, 903, 43

Eastman, J. D., Rodriguez, J. E., Agol, E., et al. 2019, arXiv:1907.09480

Fullerton, A. W., Massa, D. L., & Prinja, R. K. 2006, ApJ, 637, 1025

Gaia Collaboration 2020, yCat, 1350, 0

Garmany, C. D., Olson, G. L., van Steenberg, M. E., & Conti, P. S. 1981, ApJ, 250, 660

Gies, D. R., & Bolton, C. T. 1986, ApJS, 61, 419

Glatzel, W. 1998, A&A, 339, L5

Gott, J. R. 1971, Natur, 234, 342

Gray, R. O., & Corbally, J. C. 2009, Stellar Spectral Classification (Princeton, NJ: Princeton Univ. Press)

Grin, N. J., Ramírez-Agudelo, O. H., de Koter, A., et al. 2017, A&A, 600, A82

Gull, T. R., & Sofia, S. 1979, ApJ, 230, 782

Guo, Y., Wang, L., Liu, C., et al. 2024, ApJS, 272, 45

Gvaramadze, V. V., & Bomans, D. J. 2008, A&A, 490, 1071

Gvaramadze, V. V., & Gualandris, A. 2011, MNRAS, 410, 304

Gvaramadze, V. V., Kniazev, A. Y., Kroupa, P., & Oh, S. 2011a, A&A, 535, A29

Gvaramadze, V. V., Menten, K. M., Kniazev, A. Y., et al. 2014a, MNRAS, 437, 843

Gvaramadze, V. V., Miroshnichenko, A. S., Castro, N., Langer, N., & Zharikov, S. V. 2014b, MNRAS, 437, 2761

Gvaramadze, V. V., Röser, S., Scholz, R. D., & Schilbach, E. 2011b, A&A, 529, A14

Hartigan, P., Raymond, J., & Hartmann, L. 1987, ApJ, 316, 323

Heckman, T. M., Lehnert, M. D., & Armus, L. 1993, in The Environment and Evolution of Galaxies, ed. J. M. Shull & H. A. Thronson (Berlin: Springer), 455

Helfand, D. J., Gotthelf, E. V., & Halpern, J. P. 2001, ApJ, 556, 380

Henden, A. A., Templeton, M., Terrell, D., et al. 2016, yCat, 2336, 0

Herrero, A., Kudritzki, R. P., Vilchez, J. M., et al. 1992, A&A, 261, 209

Holgado, G., Simón-Díaz, S., Herrero, A., & Barbá, R. H. 2022, A&A, 665, A150

Hoogerwerf, R., de Bruijne, J. H. J., & de Zeeuw, P. T. 2000, ApJL, 544, L133

Houk, N. 1982, Michigan Catalogue of Two-dimensional Spectral Types for the HD Stars. Volume_3. Declinations −40_f0 to −26_f0 (Ann Arbor, MI: Univ. Michigan)

Howarth, I. D., & Prinja, R. K. 1989, ApJS, 69, 527

Howarth, I. D., & Smith, K. C. 2001, MNRAS, 327, 353

Huang, W., Gies, D. R., & McSwain, M. V. 2010, ApJ, 722, 605

Hubeny, I., & Lanz, T., 2011 Synspec: General Spectrum Synthesis Program, Astrophysics Source Code Library, ascl:1109.022

Irrgang, A., Przybilla, N., Heber, U., et al. 2014, A&A, 565, A63

Jayasinghe, T., Dixon, D., Povich, M. S., et al. 2019, MNRAS, 488, 1141

Kaper, L., van Loon, J. T., Augusteijn, T., et al. 1997, ApJL, 475, L37

Klein, R. I., & Castor, J. I. 1978, ApJ, 220, 902

Kobulnicky, H. A., & Chick, W. T. 2022, yCat, J/AJ/164/86

Kobulnicky, H. A., Chick, W. T., & Povich, M. S. 2018, ApJ, 856, 74

Kobulnicky, H. A., Chick, W. T., & Povich, M. S. 2019, AJ, 158, 73

Kobulnicky, H. A., Chick, W. T., Schurhammer, D. P., et al. 2016, ApJS, 227, 18

Kobulnicky, H. A., Gilbert, I. J., & Kiminki, D. C. 2010, ApJ, 710, 549

Kobulnicky, H. A., Kiminki, D. C., Lundquist, M. J., et al. 2014, ApJS, 213, 34

Körtgen, B., Seifried, D., Banerjee, R., Vázquez-Semadeni, E., & Zamora-Avilés, M. 2016, MNRAS, 459, 3460

Krtička, J., Kubát, J., & Krtičková, I. 2021, A&A, 647, A28

Krumholz, M. R., & Tan, J. C. 2007, ApJ, 654, 304

Lamb, J. B., Oey, M. S., Segura-Cox, D. M., et al. 2016, ApJ, 817, 113

Lamers, H. J. G. L. M., & Leitherer, C. 1993, ApJ, 412, 771

Langer, N. 1997, in ASP Conf. Ser. 120, Luminous Blue Variables: Massive Stars in Transition, ed. A. Nota & H. Lamers (San Francisco, CA: ASP), 83

Langer, N. 1998, A&A, 329, 551

Langer, N. 2012, ARA&A, 50, 107

Langer, N., & Kudritzki, R. P. 2014, A&A, 564, A52

Lanz, T., & Hubeny, I. 2003, ApJS, 146, 417

Lanz, T., & Hubeny, I. 2007, ApJS, 169, 83

Lee, C.-F., Mundy, L. G., Reipurth, B., Ostriker, E. C., & Stone, J. M. 2000, ApJ, 542, 925

Leitherer, C. 1988, ApJ, 326, 356

Leonard, P. J. T. 1991, AJ, 101, 562

Liu, Z., Cui, W., Liu, C., et al. 2019, ApJS, 241, 32

Mahy, L., Rauw, G., De Becker, M., Eenens, P., & Flores, C. A. 2015, A&A, 577, A23

Majewski, S. R., Zasowski, G., & Nidever, D. L. 2011, ApJ, 739, 25

Malkov, O. Y., Oblak, E., Snegireva, E. A., & Torra, J. 2006, A&A, 446, 785

Marcolino, W. L. F., Bouret, J. C., Martins, F., et al. 2009, A&A, 498, 837

Markova, N., & Puls, J. 2008, A&A, 478, 823

Massa, D., Fullerton, A. W., & Prinja, R. K. 2017, MNRAS, 470, 3765

Mellon, S. N., Mamajek, E. E., Stuik, R., et al. 2019, ApJS, 244, 15

Mugnes, J. M., & Robert, C. 2015, MNRAS, 454, 28

Negueruela, I., Simón-Díaz, S., de Burgos, A., Casasbuenas, A., & Beck, P. G. 2024, A&A, 690, A176

Nieva, M. F., & Przybilla, N. 2012, A&A, 539, A143

Noriega-Crespo, A., van Buren, D., Cao, Y., & Dgani, R. 1997a, AJ, 114, 837

Noriega-Crespo, A., van Buren, D., & Dgani, R. 1997b, AJ, 113, 780

Olivier, G. M., Lopez, L. A., Rosen, A. L., et al. 2021, ApJ, 908, 68

Pecaut, M. J., & Mamajek, E. E. 2013, ApJS, 208, 9

Perets, H. B., & Šubr, L. 2012, ApJ, 751, 133

Peri, C. S., Benaglia, P., & Isequilla, N. L. 2015, A&A, 578, A45

Pflamm-Altenburg, J., & Kroupa, P. 2010, MNRAS, 404, 1564

Phillips, G. D., Oey, M. S., Cuevas, M., Castro, N., & Kothari, R. 2024, ApJ, 966, 243

Poveda, A., Ruiz, J., & Allen, C. 1967, BOTT, 4, 86

Povich, M. S., Benjamin, R. A., Whitney, B. A., et al. 2008, ApJ, 689, 242

Puls, J., Kudritzki, R. P., Herrero, A., et al. 1996, A&A, 305, 171

Renzo, M., Zapartas, E., de Mink, S. E., et al. 2019, A&A, 624, A66

Rivero González, J. G., Puls, J., Massey, P., & Najarro, F. 2012, A&A, 543, A95

Rubio-Díez, M. M., Sundqvist, J. O., Najarro, F., et al. 2022, A&A, 658, A61

Ryans, R. S. I., Dufton, P. L., Rolleston, W. R. J., et al. 2002, MNRAS, 336, 577

Sana, H., & Evans, C. J. 2011, in IAU Symp. 272, Active OB Stars: Structure, Evolution, Mass Loss, and Critical Limits, ed. C. Neiner et al. (Cambridge: Cambridge Univ. Press), 474

Sana, H., Ramírez-Agudelo, O. H., Hénault-Brunet, V., et al. 2022, A&A, 668, L5

Shepard, K., Gies, D. R., Kaper, L., & De Koter, A. 2022, ApJ, 931, 35

Simón-Díaz, S., Castro, N., Garcia, M., Herrero, A., & Markova, N. 2011, BSRSL, 80, 514

Simón-Díaz, S., Godart, M., Castro, N., et al. 2017, A&A, 597, A22

Sota, A., Maíz Apellániz, J., Walborn, N. R., et al. 2011, ApJS, 193, 24

Stapelfeldt, K. R., Beichman, C. A., Hester, J. J., Scoville, N. Z., & Gautier, T. N., III 1991, ApJ, 371, 226

Stone, R. C. 1979, ApJ, 232, 520

van Buren, D., & McCray, R. 1988, ApJL, 329, L93

van den Heuvel, E. P. J., & Heise, J. 1972, NPhS, 239, 67

van Rensbergen, W., Vanbeveren, D., & De Loore, C. 1996, A&A, 305, 825

Verhamme, O., Sundqvist, J., de Koter, A., et al. 2024, A&A, 692, A91

Villamariz, M. R., & Herrero, A. 2000, A&A, 357, 597

Vink, J. S., de Koter, A., & Lamers, H. J. G. L. M. 2001, A&A, 369, 574

Wang, Z., Kaplan, D. L., Slane, P., Morrell, N., & Kaspi, V. M. 2013, ApJ, 769, 122

Webster, B. L., & Murdin, P. 1972, Natur, 235, 37

Weßmayer, D., Przybilla, N., & Butler, K. 2022, A&A, 668, A92

Zwicky, F. 1957, ZA, 44, 64